Environmental Science and Pollution Research (2019) 26:12379–12398
https://doi.org/10.1007/s11356-019-04625-0

RESEARCH ARTICLE

Controllable synthesis of Fe_3O_4-wollastonite adsorbents for efficient heavy metal ions/oxyanions removal

Jelena D. Rusmirović[1] · Nina Obradović[2] · Jovana Perendija[3] · Ana Umićević[4] · Ana Kapidžić[4] · Branislav Vlahović[5] · Vera Pavlović[6] · Aleksandar D. Marinković[7] · Vladimir B. Pavlović[2,8]

Received: 20 November 2018 / Accepted: 19 February 2019 / Published online: 7 March 2019

Abstract

Iron oxide, in the form of magnetite (MG)–functionalized porous wollastonite (WL), was used as an adsorbent for heavy metal ions (cadmium and nickel) and oxyanions (chromate and phosphate) removal from water. The porous WL was synthesized from calcium carbonate and siloxane by controlled sintering process using low molecular weight submicrosized poly(methyl methacrylate) as a pore-forming agent. The precipitation of MG nanoparticles was carried out directly by a polyol-medium solvothermal method or via branched amino/carboxylic acid cross-linker by solvent/nonsolvent method producing WL/MG and WL-γ-APS/MG adsorbents, respectively. The structure/properties of MG functionalized WL was confirmed by applying FTIR, Raman, XRD, Mössbauer, and SEM analysis. Higher adsorption capacities of 73.126, 66.144, 64.168, and 63.456 mg g^{-1} for WL-γ-APS/MG in relation to WL/MG of 55.450, 52.019, 48.132, and 47.382 mg g^{-1} for Cd^{2+}, Ni^{2+}, phosphate, and chromate, respectively, were obtained using nonlinear Langmuir model fitting. Adsorption phenomena were analyzed using monolayer statistical physics model for single adsorption with one energy. Kinetic study showed exceptionally higher pseudo-second-order rate constants for WL-γ-APS/MG, e.g., 1.17–13.4 times, with respect to WL/MG indicating importance of both WL surface modification and controllable precipitation of MG on WL-γ-APS.

Keywords Calcium metasilicate ceramic · Magnetite functionalization · Solvent/nonsolvent method · Polyol-thermal method · Heavy metals · Adsorption; Fe_3O_4

Introduction

Rapid global industrialization increases the amount of effluent consisting chemical wastes such as volatile organic compounds (industrial solvents), heavy metals and oxyions, and pharmaceutical drugs and their metabolites. Industrial effluents are one of the prime sources of environmental toxicity that deteriorates water quality (Paul 2017). Long-term

Responsible editor: Tito Roberto Cadaval Jr

Electronic supplementary material The online version of this article (https://doi.org/10.1007/s11356-019-04625-0) contains supplementary material, which is available to authorized users.

✉ Jelena D. Rusmirović
jrusmirovic@tmf.bg.ac.rs

[1] Innovation Center of the Faculty of Technology and Metallurgy, University of Belgrade, Karnegijeva 4, Belgrade 11120, Serbia

[2] Institute of Technical Sciences of SASA, Knez Mihailova 35/IV, Belgrade 11000, Serbia

[3] Institute of Chemistry, Technology and Metallurgy, University of Belgrade, Njegoševa 4, Belgrade 11000, Serbia

[4] Vinča Institute of Nuclear Sciences, University of Belgrade, Belgrade, Serbia

[5] Department of Mathematics and Physics, North Carolina Central University, Durham, USA

[6] Faculty of Mechanical Engineering, University of Belgrade, Kraljice Marije 16, Belgrade 11120, Serbia

[7] Faculty of Technology and Metallurgy, University of Belgrade, Karnegijeva 4, Belgrade 11120, Serbia

[8] Faculty of Agriculture, University of Belgrade, Nemanjina 6, Belgrade-, Zemun 11080, Serbia

exposure to heavy metals, such as cadmium, nickel, and chromium (Cd^{2+}, Ni^{2+}, and Cr(VI)), by ingestion/inhalation leads to a buildup in kidneys and possible kidney disease, lung damage, cancer, and fragile bones (Karthikeyan et al. 2005; Martin and Griswold 2009). Due to that, Environmental Protection Agency (EPA) limits concentration of Cd^{2+} to 0.005 ppm and of Ni^{2+} and Cr(VI) to 0.1 ppm in water (EPA 2014). As an essential nutrient required for critical biological reactions maintaining the normal homoeostatic control of the cell, and growth of algae, phosphorus is an important component of different cellular structures (Mezenner and Bensmaili 2009; Razzaque 2011). Phosphorus concentration has to be limited in order to control algal blooming (Mezenner and Bensmaili 2009). The phosphate discharge standard of wastewater is averaged on 1–2 ppm in order to satisfy the stringent EPAs limit of phosphorous concentration in natural water (0.02 ppm) (Rout et al. 2015, 2016). With the aim to maintain the pollutant concentration within the permissible limits, purification/pollutant removal from industrial water becomes imposed as a solution for susceptibility environmental toxicity.

In recent years, a great attention was directed in the development of physically and chemically removing heavy metals from contaminated water by a variety of methods, including membrane separation, flocculation, adsorption, ion-exchange, precipitation, evaporation, and electrolysis (D'Halluin et al. 2017; Iannazzo et al. 2017; Han et al. 2018). Due to low operational cost and high efficiency in the removal of many heavy metal ions, as well as the possibility of using natural materials as adsorbents, the adsorption stands out as one of the most efficient and widely used techniques for the removal of metal ions (Zeng et al. 2015). Development of the more effective and cheaper adsorbents, that may be of mineral, organic, or biological origin, has been studied in the recent decade (Abdel-Halim and Al-Deyab 2011; Zeng et al. 2015). Calcium silicates have received considerable attention as adsorbent for heavy metal adsorption due to their excellent bioactivity and biocompatibility (Chen et al. 2008; Zhao et al. 2014). Wollastonite (WL) is a naturally occurring and cheap α-calcium metasilicate (α-$CaSiO_3$) that is commonly used in preparing ceramic bodies and other materials, but lately have used as an adsorbent in water pollution control (Sharma et al. 1990a, b, 2007; Sharma 2001; Obradović et al. 2017a). Calcium oxide (CaO) and silicon dioxide (SiO_2) are the main constituents of WL ($CaO/SiO_2 = 48.18\%/48.52\%$ by weight) that can be responsible for heavy metals' adsorption (Sharma 2001). Sharma et al. (1990a, b, 2007) investigated the ability of natural WL to remove Cd^{2+}, Ni^{2+}, and Cr(VI) ions from water and found maximum removal of 93.6% and 69.5% for Cd^{2+} and Cr(VI) ions, respectively, and maximum adsorption capacity of 6.52 mg g^{-1} for Ni^{2+} ions. The main disadvantage of WL for use as an adsorbent for the removal of pollutants from aquatic systems is the hydrophilicity of its surface. Surface modification, as a key process in functional WL preparation, renders hydrophilic WL surface hydrophobic (Ding et al. 2011). In order to reduce the hydrophilicity of the WL surface and, therefore, increase the heavy metal ions' adsorption capacity, it is necessary to functionalize its surface.

Iron oxide– and oxide-hydroxide-based adsorbents have been widely used in water treatment systems for the removal of ionic pollutants (Markovski et al. 2014a, b; Taleb et al. 2015, 2016a; Lin et al. 2017; Zeng et al. 2017). Due to expressed electrostatic attraction and ligand exchange with heavy metal ions, magnetite (MG – Fe_3O_4) nanoparticles were shown to be highly efficient materials for heavy metal ion removal by adsorption (Kalantari et al. 2014). Besides, using MG in the production hybrid adsorbents resolves separation problems because, due to their magnetic property, MG particles can be easily separated from aqueous solutions using an external magnetic field (Kalantari et al. 2014). Moreover, amination of MG surface helps in the formation of uniform Fe_3O_4 deposit without appreciable nanoparticle aggregation. In that way, improvement of two benefits was achieved: controllable MG precipitation due to the strong metal chelation of amine groups and improved adsorption performances of the obtained adsorbent (Qi et al. 2017). To the best of our knowledge, there are no examples in the literature dealing with the removal of Cd^{2+}, Ni^{2+}, chromate, and phosphate ions by WL-based adsorbent with impregnated MG particles.

Besides the adsorbent morphology and surface properties, the operating conditions play an important role in achieving high adsorption capacities. Many theoretic studies (isothermal, kinetic, statistical-physic models) are carried out to understand the behavior of single-compound adsorption systems since the operating conditions can be potentially infinite in terms of combination of pollutant concentration, temperature, and time of the pollutant/adsorbent contact (Sellaoui et al. 2016a, b, 2017a, b). Freundlich and Langmuir models are mostly used to analyze the adsorption equilibrium of heavy metal removal using WL- or MG-based adsorbents in a single component system (Sharma et al. 1990a, b, 2007; Taleb et al. 2016b; Obradović et al. 2017a, b). More precise interpretation of single adsorption isotherm can be obtained using statistical physic theory, etc., monolayer models with one or two energies. The obtained theoretical results connect experimental result with successfulness of the applied adsorbent synthesis process and operation conditions.

In the present work, the ability of a hybrid material consisting of the WL as a support of MG particles, for the removal of Cd^{2+}, Ni^{2+}, chromate, and phosphate ions from aqueous solutions, was studied. The ions' adsorption capacity of the WL impregnated with MG can be controlled either by direct precipitation of MG particles or polyol-medium solvothermal method and via (3-aminopropyl)trimethoxysilane cross-linker by solvent/nonsolvent system method. The adsorption experiments were performed in order to analyze the

influence of the MG precipitation method, adsorbent amount, adsorption temperature, and contact time on achieved capacities. Moreover, the present work is a modeling study of heavy metal ion/oxyanions' removal and provides useful information about the adsorption mechanisms in single-compound system.

Experimental section

Materials

All reagents were of analytical grade and used without purification. Deionized water (DW), of resistivity of 18 MΩcm, was used. Ultrapure HNO_3 acid and diethylenetriaminepentaacetic acid (DETAPAA) were supplied from Fluka. Iron(III) chloride hexahydrate ($FeCl_3 \cdot 6H_2O$), iron(II) sulfate heptahydrate ($FeSO_4 \cdot 7H_2O$), sodium hydrogen carbonate ($NaHCO_3$), sodium acetate (NaAc), polyethylene glycol 6000 (PEG-6000), (3-aminopropyl)triethoxysilane, methanol, methyl methacrylate (MMA), potassium persulfate, calcium carbonate ($CaCO_3$), *N*,*N*-dimethylformamide (DMF), toluene, and isopropyl alcohol were supplied from Sigma-Aldrich. Methylhydrocyclosiloxane was supplied from abcr GmbH. Standard solutions of nickel(II) nitrate hexahydrate (1000 ppm) was supplied from Accustandard. Cadmium(II) nitrate tetrahydrate (1000 ppm) was supplied from Panreac. Chromium(VI) standard for ICP (1000 ppm) was supplied from Sigma-Aldrich. Phosphate standard solution (1000 pm) was supplied from Merck KGaA.

Synthesis of submicro-poly(methyl methacrylate) spheres

Synthesis of submicro-poly(methyl methacrylate) (PMMA) spheres was done according to the procedure described elsewhere (Shim et al. 2004). Polymerization was carried out in a 250-mL three-necked glass reactor equipped with a magnetic stirrer (stirring rate, 100 rpm), reflux condenser, nitrogen inlet tube, and an oil bath. Mixture of 100 mL of methanol and 50 mL water was added in the glass reactor followed by addition of 5 g of MMA, and the temperature was raised up to 70 °C. Thereafter, the aqueous potassium persulfate (KPS) solution (0.0375 g of KPS in 10 mL of water) was added, and the polymerization was initiated under nitrogen (inert) atmosphere at 70 °C. After 1 h, the mixture was cooled down using an ice-bath, and PMMA was washed three times with a cold methanol/water mixture (90/10 *v*/*v*) by applying repeated centrifugation/ultrasound treatment.

Synthesis of diethylenetriaminepentaacetic acid dianhydride

Synthesis of diethylenetriaminepentaacetic acid dianhydride (DETAPADA) was done according to the procedure described elsewhere (Capretta et al. 1995). In a dry three-necked glass reactor equipped with a magnetic stirrer, reflux condenser, nitrogen inlet tube, and calcium chloride protection tube, immersed in an oil bath, 23.6 g of DETAPAA (60.0 mmol) was suspended in 31 mL of dry pyridine followed by addition of 24 mL of acetic anhydride. The mixture was heated at 65 °C for 24 h under intensive mixing, cooled down, and filtered under vacuum and inert atmosphere. The obtained product, white solid, was collected and washed with 200 mL of acetic anhydride and 200 mL of diethyl ether and dried under vacuum at 50 °C for 6 h.

Synthesis of wollastonite-based adsorbent

Wollastonite-based adsorbents were synthesized in a two-step pressureless sintering process described in the previous research (Obradović et al. 2017a). In the first step, 7.79 g methylhydrocyclosiloxane was dissolved in 100 mL of isopropyl alcohol under magnetic stirring at ambient temperature. Thereafter, 9 g of micro-sized $CaCO_3$ was added and mixed for 10 min, followed by ultrasound treatment (Bandelin electronic ultrasonic bath, Berlin, Germany; power 120 W, frequency 35 kHz) for 20 min and dried overnight at 80 °C. The obtained paste was calcined in a furnace at 250 °C during 30 min, with a 5 °C/min heating rate. In the second step, the as-prepared wollastonite powder (0.80 g) was carefully homogenized with a pore-forming agent (0.20 g submicro-PMMA spheres), molded in a cylinder pallet (dimension, 5 mm·ϕ10), and sintered at 900 °C for 1 h, with a 5 °C/min heating rate.

Direct attaching of MG spheres on wollastonite

The generation of MG nanoparticles was carried out by a polyol-medium solvothermal method according to the literature description (Wang et al. 2011). In single-necked glass reactor of 50 mL, 0.405 g of $FeCl_3 \cdot 6H_2O$ was dissolved into 20 mL ethylene glycol, producing an orange solution. One gram of sintered wollastonite was homogeneously dispersed applying sonication for 3 h. Addition of NaAc (1.8 g) and PEG-6000 (0.5 g), keeping a constant mechanical stirring at 800 rpm for 30 min, provided pH and viscosity adjustment of the dispersion. The obtained viscous product was transferred in a Teflon-lined stainless steel autoclave of 80 mL capacity followed by heating at 200 °C for 8 h. The black precipitates, obtained after cooling the reaction mixture, were washed with water and ethanol three times and dried in a vacuum oven at 60 °C. The final product was labeled WL/MG.

Attachment of MG nanoparticles on branched carboxyl-functionalized wollastonite

Stepwise synthesis of amino-functionalized and subsequently carboxy terminal functionalization of WL was performed by applying the modified literature method (Taleb et al. 2015). Amino group functionalization of WL was achieved by a direct silanization of WL with (3-aminopropyl)triethoxysilane (γ-APS). The product was named WL-γ-APS. In a 100-mL three-necked glass reactor, equipped with a magnetic stirrer, reflux condenser, nitrogen inlet tube, and an oil bath for heating, 1.0 g of WL was dispersed into 50 mL of toluene under continuous stirring, then 1.0 mL of triethylamine and 1.0 mL of γ-APS were added into the suspension, followed by refluxing at 80 °C for 12 h under a nitrogen atmosphere. WL-γ-APS was purified by washing in ethanol, dried under vacuum at 60 °C, and then used for carboxylic acid modification in order to obtain more reactive centers for MG precipitation. The quantitative Kaiser test (Sarin et al. 1981) predicted the concentration of terminal amino functions present on the WL-γ-APS material to be 2.50 mmol g^{-1}. Modified WL-γ-APS (1.2 g) was dispersed in 10 mL of DMF under stirring, and after, 10 mL of 0.1 mol L^{-1} solution of DETAPADA was added into the suspension, and mixed at room temperature for 24 h. Finally, the product (WL/DA) was dried under vacuum at 60 °C and used for attaching of MG spheres according to the procedure described elsewhere in the literature (Taleb et al. 2015). The acidic site concentrations were determined using the Boehm titration method (Boehm 1994), and the determined acid value for WL/DA was found to be 4.3 mmol g^{-1}.

In the last step, WL/DA (1.3 g) was sonicated in 30 mL of toluene with simultaneous introduction of nitrogen for 30 min, and after, pH of dispersion was adjusted at ~ 6. The reaction was continued by dropwise addition of 1.0 mL of 0.125 mol L^{-1} $FeSO_4 \cdot 7H_2O$ solution for 15 min under magnetic stirring and inert atmosphere. Neutralization of the reaction mixture with a 1 mol L^{-1} $NaHCO_3$ buffer solution causes precipitation of iron oxide in the MG form. The reaction took place by heating at 90 °C for 48 h while a black product was obtained. The obtained product was filtered, washed with 200 mL DW, and dried applying vacuum/drying treatment at 60 °C/2000 Pa for 6 h. The final product was named WL-γ-APS/MG. Schematic illustration of WL modification methods is shown in Fig. 1.

Adsorption and kinetic experiments

Batch adsorption experiments of Cd^{2+}, Ni^{2+}, Cr(VI), and phosphate ions' removal, under mixing using a laboratory shaker (Digital Heating Shaking Drybath by Thermo SCIENTIFIC), were applied to determine the adsorption capacities and investigate the effects of diffusional processes on the performance of synthesized adsorbents. An appropriate adsorbent mass (m = 1.0, 1.5, 2.5, 5.0, 7.5, and 10 mg) was placed in glass vials containing 10 mL of the standard solutions of ions of interest (Cd^{2+}, Ni^{2+}, Cr(VI), and phosphate ions) at initial concentrations, C_i, of 10 ppm. According to the determined values of the point of zero charge of the WL-based adsorbents and the ion distribution, the pH values of the solutions of Cd^{2+} and Ni^{2+} ions were set at 7.5 and for the solutions of Cr(VI) and phosphate ions were set at 6.5. The adsorption and kinetic experiments were performed at 298, 308, and 318 K. The adsorption kinetic was studied by varying the adsorbent/ion contact time in the range 5–90 min at C_i = 10 ppm. The adsorption capacities of Cd^{2+}, Ni^{2+}, Cr(VI), and phosphate ions' removal using WL-based adsorbents were calculated according to the following (Eq. (1)):

$$q = \left({}^{(C_i - C_f)} \Big/ {}_{m} \right) V \quad (1)$$

where q is the adsorption capacity in mg g^{-1}, C_i and C_f are the initial and final concentrations of ions in ppm, V is the volume of solution in L, and m is the mass of the adsorbent in g. After adsorption experiments, WL/MG and WL-γ-APS/MG adsorbents were washed with DW. Further, in order to evaluate the adsorbent regeneration capabilities, wet adsorbents were redispersed in 20 mL of solution for regeneration (NaOH/NaCl, 0.5/0.5 mol L^{-1}) (Taleb et al. 2016b). The amount of desorbed ions in effluent water was measured after mixing by the laboratory shaker for 3 h in a batch system. Three consecutive adsorption/desorption cycles were performed.

Characterization method

Fourier transform infrared spectroscopy (FTIR) spectra of the WL-based adsorbents were recorded in the absorbance mode using a Nicolet™ iS™10 FT-IR Spectrometer (Thermo Fisher SCIENTIFIC) with Smart iTR™ Attenuated Total Reflectance (ATR) sampling accessories, within the range of 400–4000 cm^{-1}, at a resolution of 4 cm^{-1} and in 20 scan modes.

The X-ray powder diffraction patterns were obtained using a Philips PW-1050 diffractometer with λ Cu–K_α radiation and a step/time scan mode of 0.05 ° s^{-1}. The measurements were taken at room temperature in air.

The morphology of the sintered powders was characterized by the scanning electron microscopy (JEOL JSM-6390 LV). The pallets were crushed and covered with gold in order to perform these measurements.

Raman spectra of the WL-based adsorbent, recorded in the range 200–1200 cm^{-1}, were collected with a Horiba Jobin Yvon Aramis Raman/PL System. The system employed a 633-nm laser (output power 4 mW, on sample 1 mW). All the measurements were realized using a spectrometer

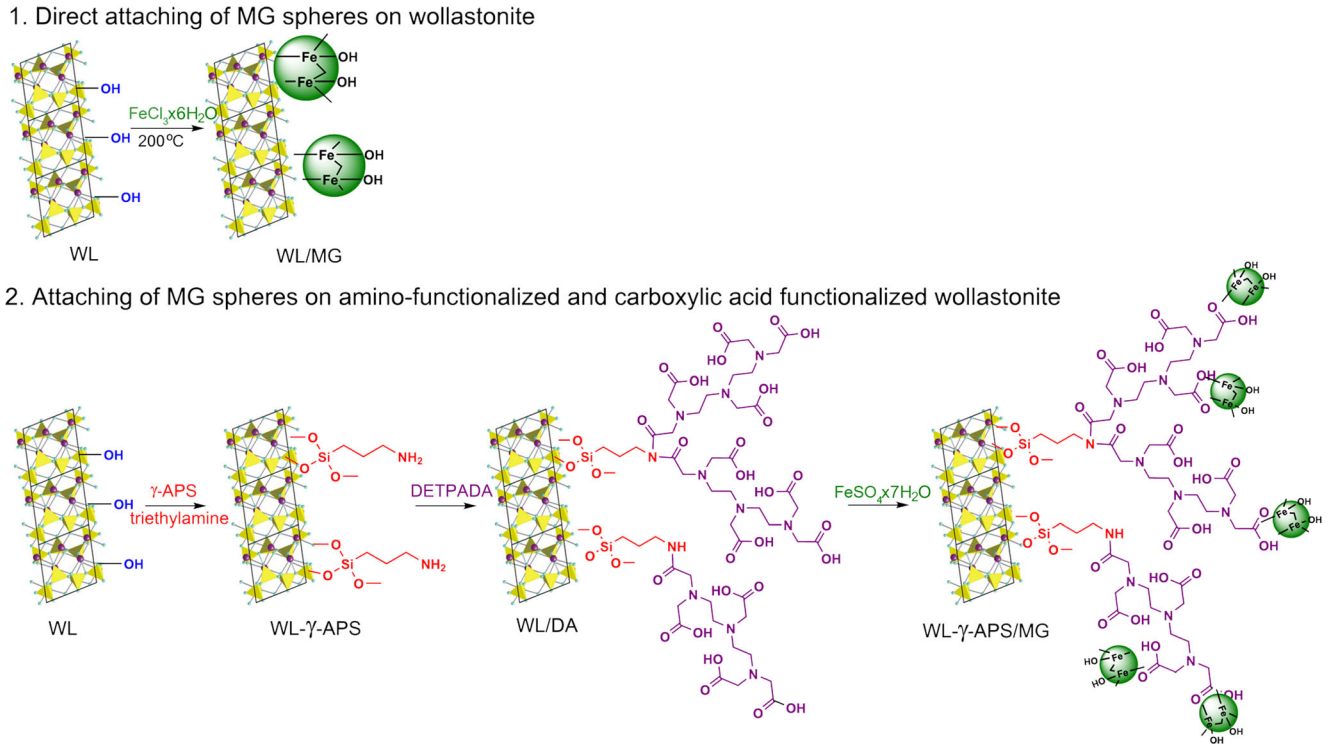

Fig. 1 Schematic illustration of 1) direct attaching of MG spheres on WL and 2) attaching of MG spheres on amino/carboxylic acid–functionalized WL

equipped with 1800 lines mm^{-1}, microscope objective of ×100, and acquisition of 10 s per 30 cycles.

The ^{57}Fe-Mössbauer spectra were obtained at room temperature in the standard transmission geometry in the constant acceleration mode using a ^{57}Co(Rh) radioactive source. The velocity scale was calibrated by the spectrum of alpha iron foil. The Mössbauer spectra were fitted by WinNormos software package (Brand 2008). The isomer shift values (δ) are given relative to α-Fe ($\delta = 0$).

The Cd^{2+}, Ni^{2+}, Cr(VI), and phosphate ions' concentrations in the solutions after the adsorption and kinetic experiments were analyzed by a PinAAcle 900T Atomic Absorption Spectrometer. The mean value from the three adsorption experiments was used for the processing of experimental data.

Results and discussion

ATR-FTIR analysis

ATR-FTIR spectra of the unmodified and MG-modified WL-based adsorbents are shown in Fig. 2. The bands' characteristic for WL containing ceramics observed at 994 cm^{-1} and 1110 cm^{-1} originates from stretching bridging Si–O (Si) vibrations, while bands at 897 cm^{-1}, 874 cm^{-1}, and 846 cm^{-1} originate from stretching non-bridging Si–O vibrations (Obradović et al. 2017a). The low intensity band at 714 cm^{-1} originates from stretching vibration of Si–O (Si) bridging bond, which is characteristic for the presence of a 3-membered ring in WL ceramics. The intense band at 1410 cm^{-1} is assigned to the carbonate ion vibrational modes in bulk calcite. Broad band around 3300–3500 cm^{-1}, observed in ATR-FTIR spectra of WL/DA, originates from hydroxyl group (OH) stretching vibration. The bands at 2930 cm^{-1}

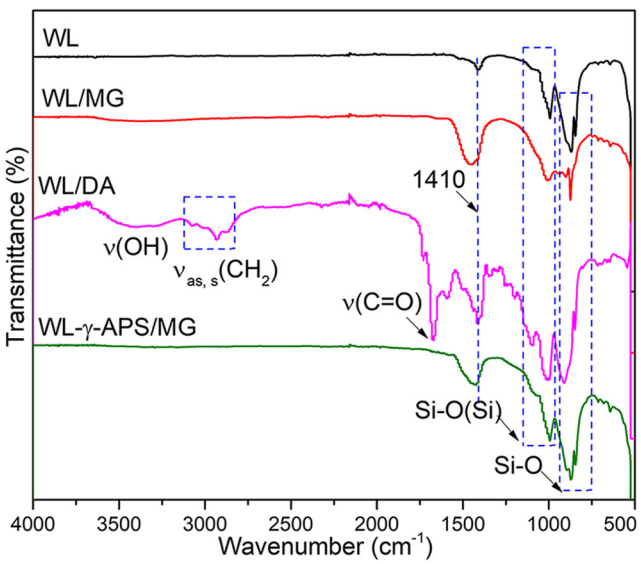

Fig. 2 ATR-FTIR spectra of modified wollastonite-based adsorbents

and 2870 cm^{-1} originate from symmetric and asymmetric stretching vibrations of methylene group. Moreover, the absorption peaks at 1680 cm^{-1} and 1580 cm^{-1} originate from amide I stretching vibrations and N–H deformation vibrations coupled with ν(C–N) vibrations (amide II), respectively.

The low intensity peak around 564 cm^{-1} observed in the ATR-FTIR spectrum of WL/MG and WL-γ-APS/MG originates from vibration of the Fe^{2+}–O^{2-} functional group (Khalil 2015) overlapped with the peaks which originate from the C–C=O and C–N–C vibrations (DETAPA moiety in WL-γ-APS/MG sample). Raman spectroscopy and ^{57}Fe-Mössbauer analysis are more suitable techniques for the quantification of the amount of MG doped on WL-containing ceramics, as well as the determination of the phase and composition of the deposit.

Raman analysis

Raman spectra of the unmodified and modified (direct/via γ-APS/DA cross-linker) WL-based adsorbents are shown in Fig. 3. In the Raman spectrum of unmodified WL, peaks that originate from both bare WL and β-larnite are noticed. The peak assignation is done according to the literature data and it is shown in Fig. 3 (Swamy et al. 1997; Richet et al. 1998; Ricciardi et al. 2009; Sokol et al. 2015). The small intensity peak at 1083 cm^{-1} indicates that there are residual $CaCO_3$ in WL structure (White 2009; Ricciardi et al. 2009).

In the Raman spectra of both modified WL samples, i.e., WL/MG and WL-γ-APS/MG, two wide peaks of magnetite, followed by two low intensity peaks of maghemite, are observed (de Faria et al. 1997; Ovsyannikov et al. 2010; Li et al. 2012). Partial transformation of magnetite into maghemite is found to induce by laser excitation (de Faria et al. 1997). The WL peaks at < 500 cm^{-1} can be assigned to the Ca–O stretching (the lowest frequencies in the region) and bending vibrations (higher frequencies in the region). On the other hand, Raman signals of WL observed between 500 and 600 cm^{-1} originate from the O–Si–O bending vibrations. Although the band at 635 cm^{-1} can be attributed to the Si–O–Si bending vibration (Osticioli et al. 2009; Buzatu and Buzgar 2010; Ebbert et al. 2014), some authors point out that this peak originates from the Si–O_{br} stretching vibrations, where O_{br} presents bridging oxygen. The stretching Si–O_{br} vibrations induce also the occurrence of the peak between 650 and 750 cm^{-1}, while Raman peaks between 850 and 200 cm^{-1} can be assigned to the Si–O non-bridging stretching vibrations (Si–O_{nbr}).

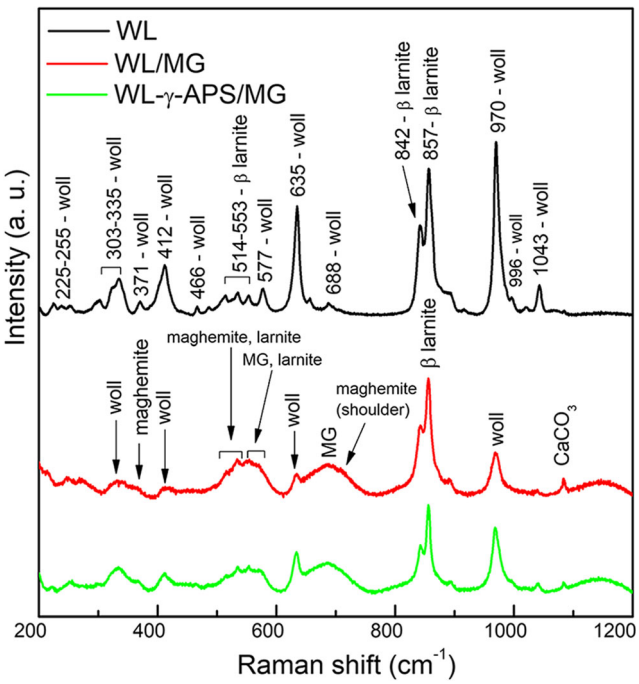

Fig. 3 Raman spectra of W-MG and W-γ-APS/MG adsorbents

XRD analysis

XRD patterns of sintered unmodified WL and modified WL samples, WL/MG and WL-γ-APS/MG, are presented in Fig. 4. All obtained intensities are identified by JCPDS cards (042-0547 for wollastonite $CaSiO_3$ and 077-0409 for larnite Ca_2SiO_4). A two-phase system is detected in the unmodified WL samples: wollastonite and larnite (13.4% $CaSiO_3$ and 86.6% Ca_2SiO_4). Peaks for magnetite, marked by their indices ((111), (220), (311), (400), (422), (511), (440)) (Wang et al. 2009; Huang et al. 2017), are observed in XRD curves for both WL/MG and WL-γ-APS/MG samples. No additional peaks are observed.

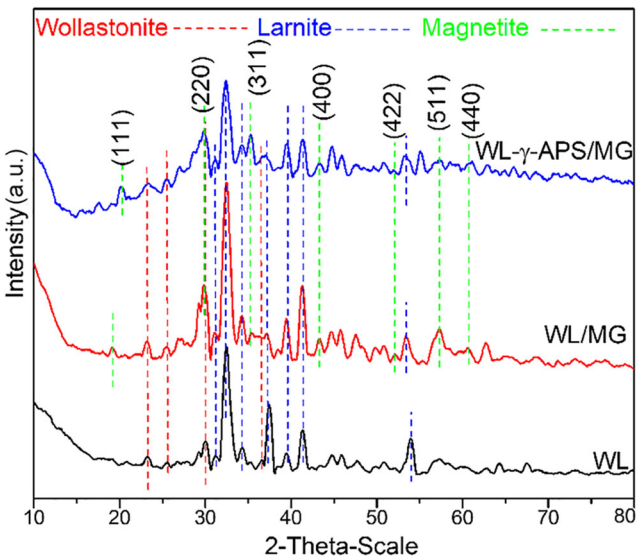

Fig. 4 XRD patterns of unmodified WL, WL/MG, and WL-γ-APS/MG samples

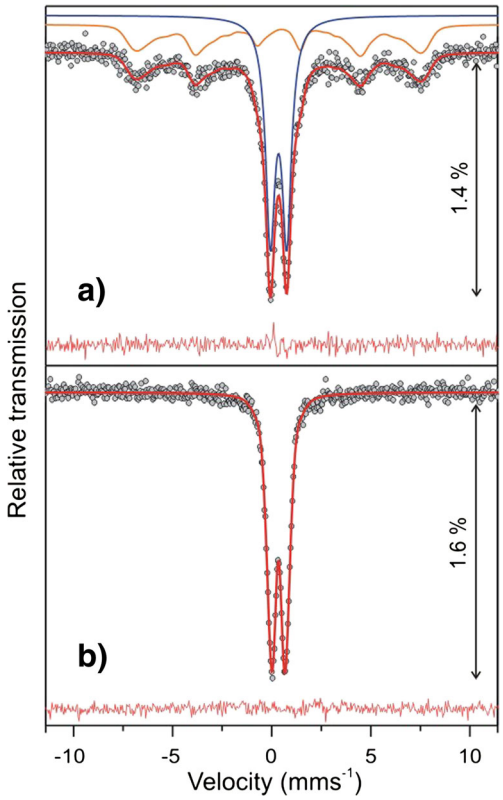

Fig. 5 Room temperature Mössbauer spectrum of the a) WL/MG and b) WL-γ-APS/MG. (On each individual plot, experimental data are presented by solid circles and the fit is given by the red solid line. Vertical arrow denotes relative position of the lowermost peak with respect to the basal line. Red solid line in the lower part of the plot represents the error calculated as the difference (Th-Exp). a) The fitted lines of the Mössbauer subspectra are plotted above the main spectrum fit: D-subspectrum (blue) and B-subspectrum (orange). The largest value of the absolute difference is less than 0.2%. b) The largest value of the absolute difference is less than 0.09%.)

^{57}Fe-Mössbauer spectroscopy

The ^{57}Fe-Mössbauer spectra of modified WL samples, WL-γ-APS/MG and WL-MG, are presented in Fig. 5. The samples were evaluated using WinNormos-DIST program. The two absorption lines (so-called a doublet) were visible in the WL-γ-APS/MG spectrum. The spectrum was fitted with the distribution of the quadrupole splitting. The distribution was described using histogram distribution of 30 doublets of Lorentzian lines with the same FWHM (0.3 mms^{-1}) in steps of 0.1 mms^{-1}. The linear correlation between the quadrupole splitting and the isomer shift was applied. Isomer shifts for the quadrupole distribution covered range from ~0.33 to ~0.34 mms^{-1}. The quadrupole splitting distribution $P(\Delta)$ of the WL-γ-APS/MG sample is presented in Fig. 6. In the WL/MG spectrum, besides the dominant central doublet, a broad six-line absorption feature (so-called a sextet) representing the magnetic contribution to the spectrum was also visible. The spectrum was fitted with one discrete doublet

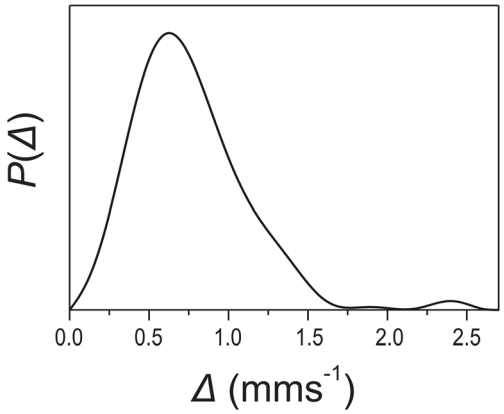

Fig. 6 The quadrupole splitting distribution $P(\Delta)$ of the WL-γ-APS/MG sample

and one distribution of the hyperfine magnetic field (distribution of the magnetic splitting). The distribution of the magnetic splitting was described using a histogram distribution of 35 sextets of Lorentzian lines with the same FWHM (0.5 mms^{-1}) from 15 T in steps of 1 T. The linear correlation between the hyperfine magnetic field and the isomer shift was applied. Isomer shifts for the magnetic distribution covered the range from ~0.32 to ~0.64 mms^{-1}. The quadrupole shift was fixed to zero. The hyperfine magnetic field distribution $P(B_{hf})$ of the magnetic part of the WL/MG sample is presented in Fig. 7. In the same DIST program, one discrete doublet was combined with the magnetic distribution. The ^{57}Fe-Mössbauer parameters of the WL/MG and WL-γ-APS/MG samples are presented in Table 1. Under the assumption that *f* factors of Fe atoms at various sites in the particular sample are identical, the area of the corresponding Mössbauer subspectrum was used to access the relative fractions of iron atoms at different sites.

The stoichiometric magnetite has an inverse spinel crystal structure. The tetrahedral sites (A-sites) are occupied by Fe^{3+} ions and the octahedral sites (B-sites) by the Fe^{3+} and Fe^{2+}

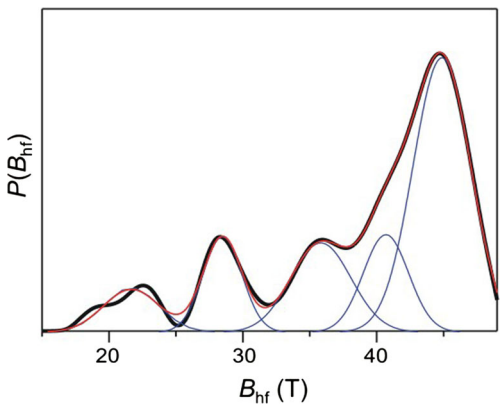

Fig. 7 Black line - hyperfine magnetic field distribution P (B_{hf}) of the magnetic part of the WL/MG spectra. Red line - fit of the $P(B_{hf})$ distribution with five Gaussian (five blue lines)

Table 1 Room temperature ^{57}Fe-Mössbauer hyperfine parameters for the WL/MG and WL-γ-APS/MG samples

Sample	Mössbauer subspectrum	A (%)	Γ (mms^{-1})	$\delta/\langle\delta\rangle$ (mms^{-1})	$\Delta/\langle\Delta(\sigma)\rangle$ (mms^{-1})	$\langle B_{hf}(\sigma)\rangle$ (T)
WL/MG	D	59	0.572 (8)	0.344 (3)	0.827 (5)	
	B-distrib.	41	0.5	0.42 (9)	0	39.1 (7.6)
WL-γ-APS/MG	Q-distrib.	100	0.3	0.339 (5)	0.76 (0.38)	

A – relative area of the Mössbauer subspectrum; Γ – line width (FWHM); δ – isomer shift; Δ – the quadrupole splitting. In the case of the distribution of the quadrupole splitting: $\langle\delta\rangle$ – average isomer shift; $\langle\Delta(\sigma)\rangle$ – average quadrupole splitting and standard deviation of the distribution of the quadrupole splitting. In case of the distribution of the magnetic splitting: $\langle\delta\rangle$ – average isomer shift; $\langle B_{hf}(\sigma)\rangle$ – average hyperfine magnetic field and standard deviation of the distribution of magnetic splitting. The fitting errors are presented in the parenthesis

ions. The site distribution in the MG structure is usually presented by the formula $(Fe^{3+})^{A}\,(Fe^{3+}\,Fe^{2+})^{B}\,O^{2-}{}_{4}$. At the temperatures above the Verwey transition temperature (~ 119 K), a rapid electron exchange exists between the Fe^{2+} and Fe^{3+} ions at the B-sites which leads to the effective $Fe^{2.5+}$ valence (Kündig and Steven Hargrove 1969, and references therein). Depending on the amount of the Fe^{2+} in the MG structure, the so-called non-stoichiometric $Fe_{3-x}O_4$ or partially oxidized MG can have a range of oxidation states (Gorski and Scherer 2010; Kalska-Szostko et al. 2015). Vacancies are formed in the MG structure (presumably on the octahedral sites) to account for the charge balance. The structure of the completely oxidized MG ($x = 1/3$) is the crystal structure of the maghemite, γ-Fe_2O_3. At room temperature (RT), only two magnetic sextets are observed in the Mössbauer spectrum of pure bulk MG (Kündig and Steven Hargrove 1969; da Costa 1995; Stevens et al. 2005; Dyar et al. 2006). The first sextet that belongs to the A-site has the hyperfine magnetic field $B_{hf} \sim 49$ T, and the isomer shift value characteristic for the Fe^{3+} ions $\delta \sim 0.27$ mms^{-1}. The second sextet comprises all the iron B-sites and, due to the electron hopping between iron B-sites, exhibits the hyperfine magnetic field $B_{hf} \sim 46$ T with lines broadened and shows an isomer shift of around $\delta \sim 0.67$ mms^{-1}—an averaged value of the isomer shift values for the Fe^{2+} and Fe^{3+} ions at B-sublattice. The ratio of the A to B sextets is 1:2. For the maghemite, the two sextets have very close values of the hyperfine magnetic fields, so only one sextet of $B_{hf} \sim 50$ T and isomer shift around $\delta \sim 0.32$ mms^{-1} is seen in the bulk maghemite Mössbauer spectrum at RT (Stevens et al. 2005; Dyar et al. 2006). For a partially oxidized MG or for the mixture of MG and maghemite, the relative intensities of the two sextets change, but the parameters remain essentially the same (Joos et al. 2016; Fock et al. 2017). The well-defined magnetic splitting for MG and maghemite is seen at RT only for particles with the grain size larger than 15 nm and can serve as a basis for their phase differentiation. For smaller particle grains, the magnetic splitting may collapse to a singlet or doublet due to the superparamagnetic relaxation or sextet may be severely broadened (Roggwiller and Kundig 1973; da Costa et al. 1998; Dézsi et al. 2008; Suzdalev et al. 2012; Carvalho et al. 2013; Kalska-Szostko et al. 2015; Joos et al. 2016; Oshtrakh et al. 2016). Also, in the RT-Mössbauer spectrum, superparamagnetic (SPM)-magnetite nanoparticles are hard to be distinguished from the other SPM-iron-oxide/iron-hydroxide nanoparticles (Joos et al. 2016).

The calcium-based silicates may be also represented by the various doublets in the Mössbauer spectra at RT (Dowty and Lindsley 1973; Stevens et al. 2005; Dyar et al. 2006). The doublets with the isomer shift values of around 1 mms^{-1} or higher that may represent Fe^{2+} ions incorporated in the calcium-silicates or silicates (Dowty and Lindsley 1973; Murad and Wagner 1998; Stevens et al. 2005; Dyar et al. 2006) could not be fitted to the WL-γ-APS/MG spectrum. In the case of the WL/MG, the Fe^{2+} doublet originated from calcium-silicates and silicates would be covered by the broadened sextet. On the other hand, the presence of the Fe^{3+} ions in silicates in the two investigated samples could not be excluded, since their Mössbauer parameters are in most cases overlapping with the ones of the SPM-iron-oxide/hydroxide nanoparticles (Murad and Wagner 1998; Stevens et al. 2005; Dyar et al. 2006). Nevertheless, despite the difficulties stated above, the most probable scenario for the two samples is that the majority of Fe is incorporated in the iron-oxide nanophase. The calcium-silicate phases present in the samples should exhibit a Fe^{2+} ion–Mössbauer signature as mentioned above, which could not be detected in significant amount for both samples. For the WL-γ-APS/MG spectrum, the fit that may distinguish between different phases in the WL-γ-APS/MG sample, i.e., the fit with two or more doublets, could not provide a unique set of Mössbauer parameters. Therefore, we decided to fit the spectrum with one quadrupole splitting distribution. The average value of the quadrupole splitting distribution was ~ 0.76 mms^{-1}. Under assumptions that the majority of iron is incorporated into the iron-oxide nanoparticles, for the WL-γ-APS/MG sample, the waste majority of the ultrafine iron-oxide nanoparticles are in the superparamagnetic state. Similar reasons apply for the RT WL/MG–^{57}Fe-Mössbauer spectrum. The dominant doublet could be fitted to the WL/MG spectrum satisfactory with only one doublet and therefore may also incorporate both, the SPM-iron-

oxides/hydroxides and/or the silicate phases. The WL/MG–^{57}Fe-Mössbauer spectrum differs from the WL-γ-APS/MG spectrum in the presence of the magnetic contribution visible as the broadened asymmetrical sextet. The fits of the magnetic part of the WL/MG spectrum with the two magnetic field distributions for A- and B-sites in MG phase were not satisfactory. Also, the fits with one discrete sextet for the A-site and one magnetic field distribution for the B-site also failed to describe the spectrum reasonably. The magnetic component which correlated with the A-site in the MG with $B_{hf} \sim$ 49 T was not present in the spectrum. Finally, the magnetic part was fitted with one hyperfine magnetic field distribution (Fig. 7). Several peaks are present in the magnetic distribution for the WL/MG sample. An attempt to fit the probability distribution $P(B_{hf})$ with five Gaussian was made (Fig. 7): the most prominent peak is located at ~ 44.9 T ($\delta \sim$ 0.36 mms^{-1}), followed by smaller maxima at 40.7 T ($\delta \sim$ 0.40 mms^{-1}), 35.8 T ($\delta \sim$ 0.45 mms^{-1}), 28.5 T ($\delta \sim$ 0.51 mms^{-1}), and 21.7 T ($\delta \sim$ 0.58 mms^{-1}). The peaks' parameters do not indicate clearly to the specific iron-oxide/iron-hydroxide phase. Besides the abovementioned reasons associated with the reducing of the particle size, there may be several other reasons for the lowering of the hyperfine magnetic field at various Fe sites in the iron-oxide nanoparticles and broadening of the spectrum lines: significant distribution in the particles size, poorly crystallized nanoparticles, inclusion of various impurities/phases into the grains, etc.

Scanning electron microscopy

The scanning electron microscopy (SEM) micrographs of the synthesized PMMA microspheres, used as a pore-forming agent, and calcined unmodified and modified WL powders are shown in Fig. 8. From Fig. 8 a, it can be observed that the soap-free emulsion polymerization produces PMMA microspheres with high uniform dimensions (≈ 700–800 nm). During the calcination of the WL powder, PMMA microspheres are subjected to degradation and evaporation which undergo swelling and cause forming of non-uniform porous structure (Fig. 8 b). Inside WL structures, noticed pores are connected, as presented in Fig. 8 b. Submicro-size PMMA particles, approximately 0.1–1.50 microns (Sreekanth Chakradhar et al. 2006; Obradović et al. 2017a), caused micro-porosity in obtained material. A comparative morphology study of direct and indirect MG-modified WL shows that smaller MG agglomerates (Fig. 8 d) were precipitated using MG spheres attaching method via γ-APS/DA cross-linker. Clearly visible MG agglomerates with higher dimensions were obtained using the polyol-medium solvothermal method (Fig. 8 c).

These results were confirmed by EDS mapping and EDS image. The obtained results are shown in Fig. 9 and Table S1. The EDS image proves the presence of the starting elements O, Si, Ca, and Fe (Fig. 9 a, b). Moreover, the elemental mapping (O and Fe elements) shows clearly that direct attaching of MG spheres on WL led to the precipitation of MG agglomerates of higher dimensions, while attaching of MG spheres via γ-APS/DA cross-linker led to a more uniform precipitation of MG particles of smaller dimensions. This can be attributed to numerous nucleation/crystallization centers (carboxylic groups/carboxylate anions) suitable for iron complexation in the initial stage, while in the course of adsorbent synthesis, MG precipitation takes place by MG crystal growth producing a large number of more uniformly distributed smaller particle size on WL/DA surface (Fig. 1). Numerous crystallization centers affect the MG loading. Hence, as shown in the results of the EDS analysis (Table S1), a higher loading of MG was bounded by precipitation via γ-APS/DA cross-linker (11.36%), while only 4.37% were bounded by direct MG precipitation. These results were corroborated by acidic dissolution in nitric acid and determination of iron content (10.66% for WL/γ-APS/DA and 4.76% for WL/MG).

Determination of the point of zero charge (pH_{PZC}) of wollastonite-based adsorbent and effect of pH on adsorption efficiency

The pH influences the state of equilibrium of ionic species and protonation/deprotonation of sorbent functional groups. The pH of the point of zero charge, pH_{PZC} for the magnetite-modified WL-based adsorbents was measured by the pH drift method. In aqueous systems, the surface of iron oxides is covered with FeOH groups that can be protonated or deprotonated and generate surface charge $FeOH_2^+$ or FeO^- at pH values below or above the point of zero charge for magnetite (pH_{PZC}), respectively (Rajput et al. 2016). Electrostatic forces between metal ion species and surface charges are responsible for adsorption (Ahmed et al. 2013; Rajput et al. 2016). The point of zero charge for magnetite is the pH value at which the surface concentrations of $FeOH^{2+}$ and FeO^- groups are equal. The measured pH_{PZC} of unmodified WL was 2.7, while pH_{PZC} of both MG-modified WL-based adsorbents was ~ 7.0. In the next step, the removal degree of Ni^{2+} and Cd^{2+} versus the initial pH (pH_i) was studied, and the obtained results are presented in Fig. S1. At low pH (lower than pH_{PZC} of MG-modified WL), sorbent surface is covered mostly with $FeOH^{2+}$ and positively charged surface functionalities. Therefore, the positively charged metal ions, Ni^{2+} and Cd^{2+}, showed low adsorption efficiency due to both the repulsive forces and the adsorption of H_3O^+ which hinder/competitively occupy adsorptive sites (Ahmed et al. 2013).

It can be noticed from Fig. S1 that, with an increase in pH from 3 to 9, the Cd^{2+} and Ni^{2+} percentage uptake increased too. In the pH range between 7 and 9, the maximum of Ni^{2+} and Cd^{2+} percentages uptake was observed (72% and 97% Cd^{2+} uptake on WL/MG and WL-γ-APS/MG, receptively,

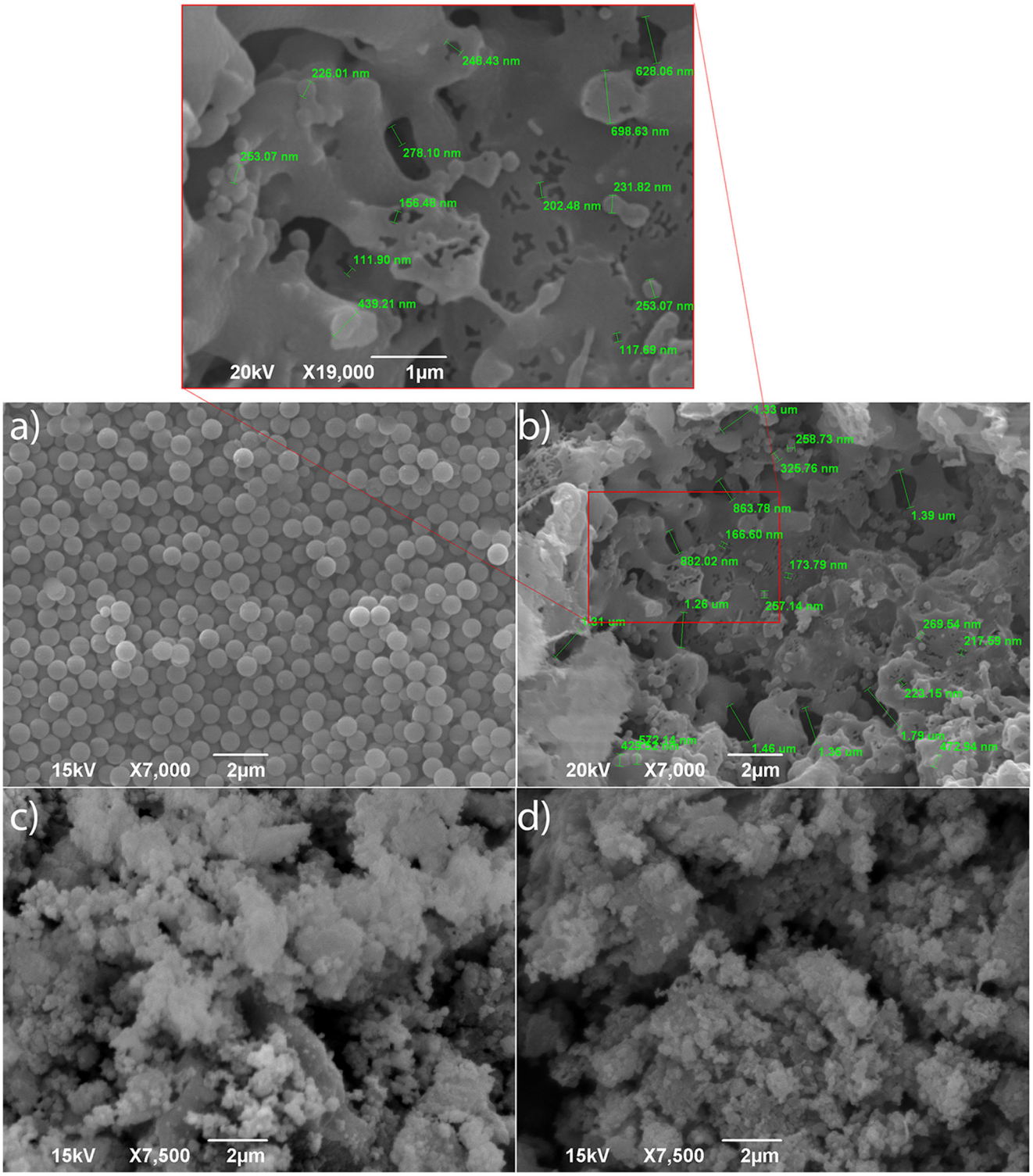

Fig. 8 SEM micrograph of synthesized **a** PMMA microsphere, **b** unmodified WL, **c** WL/MG, and **d** WL-γ-APS/MG

and 84% and 85% Ni^{2+} uptake on WL/MG and WL-γ-APS/MG, receptively). Subsequently, gradual decrease of Cd^{2+} and Ni^{2+} uptake on WL/MG and WL-γ-APS/MG was observed at pH > 8. The variation in the effectiveness of metal removal at different pH values could be explained by metal speciation as shown in Fig. S2. From the speciation diagram of Cd^{2+} and Ni^{2+} ions (Fig. S2), obtained by using MINTEQ 3.0 software (Gustafsson 2011), high removal efficiencies would be expected in the pH region 7–8 for both Cd^{2+} and Ni^{2+}, while adsorption capabilities at pH > 8 could originate from

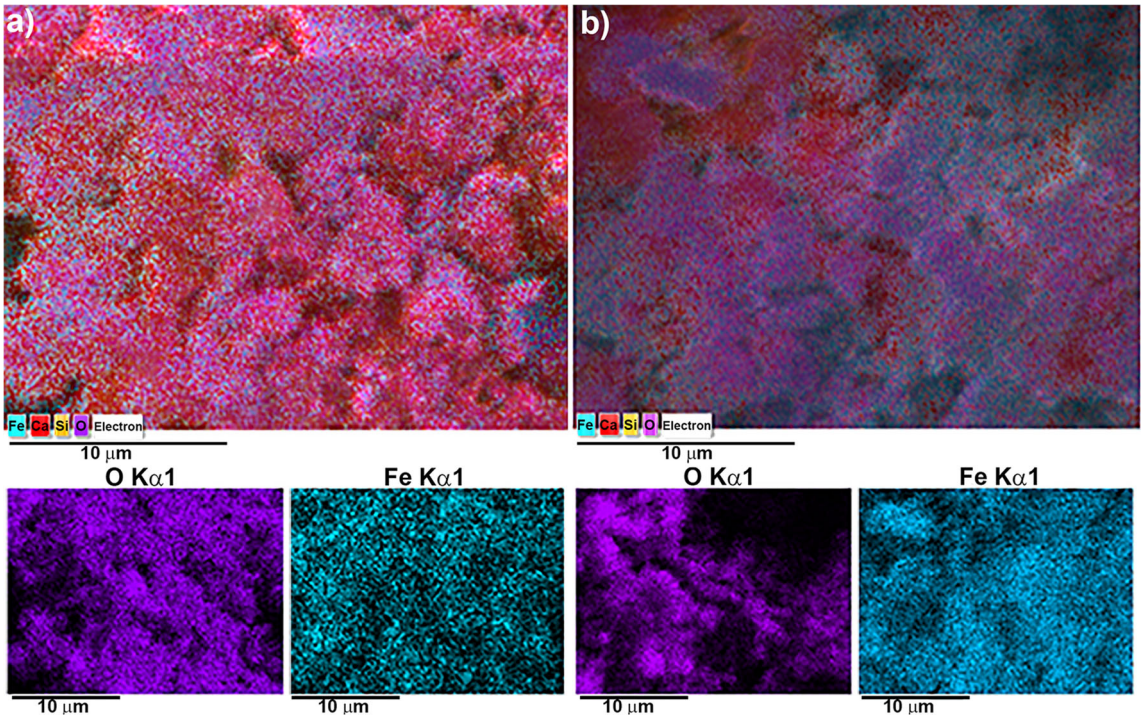

Fig. 9 EDS mapping of modified WL-based adsorbents a) WL/MG and d) WL-γ-APS/MG

additional contribution of the precipitation of insoluble metal hydroxides (Drah et al. 2017). Thus, adsorption curves for the studied cations represent only the adsorption with excluded precipitation at pH > 8. According to this, at pH < 8, it was certain that removals of Cd^{2+} and Ni^{2+} were not affected by hydroxide/salt precipitation, and obtained results were considered without any misleading conclusions (Drah et al. 2017). In this sense, the selection of pH 7.5 for Cd^{2+} and Ni^{2+} removal and pH 6.5 for both Cr(VI), considering equilibrium of $HCrO_4^-/CrO_4^{2-}$ ions, and phosphate, equilibrium of $H_2PO_4^-/HPO_4^{2-}$ ions, was an adequate choice to achieve high adsorption capacities.

Adsorption/desorption study of Cd^{2+}, Ni^{2+}, $HCrO_4^-/CrO_4^{2-}$, and $H_2PO_4^-/HPO_4^{2-}$ on WL/MG and WL-γ-APS/MG adsorbents

According to the previous adsorptions studies, it was confirmed that heavy metals undergo complexation and hydrolysis during adsorption (Kumari et al. 2015). Surface complexation of heavy metals occurs via exchange of metal ions M^{m+} with H^+ ions at the surface hydroxyl groups –M OH. $M(OH)_n^{(m-n)+}$ ions, which occurs during the hydrolysis, can electrostatically interact with the iron-oxide (MG) surfaces forming a specific type of adsorbed ion/surface interaction (Petrova et al. 2011). It was found that metals' hydrolysis causes weakening of the interaction between the metal ion and water in hydration shell that facilitates the approach of the metal ions to the surface (Petrova et al. 2011).

However, analysis/description of adsorption mechanism of oxyanions is a complex/extensive task and needs more reliable results, and most of them are based on spectroscopic evidence (Kumari et al. 2015). Multiple adsorption mechanisms occur during the phosphate ions uptaking. The cationic species ($M(OH)_n^{(m-n)+}$) takes part in the uptaking of phosphate ions via electrostatic interaction (Rout et al. 2015, 2016). However, it is proved that complexation of oxyanions on MG surface was achieved by formation of monodentate and bidentate complexes through covalent bonding between the surface oxide's oxygen and the adsorbing metal ion (Kumari et al. 2015). Three main forms of phosphate complexes on iron oxide surface were defined: protonated ($(FeO)_2(OH)PO$), non-protonated bridging bidentate ($(FeO)_2PO_2$), and a non-protonated monodentate ($(FeO)PO_3$) (Tejedor-Tejedor and Anderson 1990). In a similar manner due to similar chemistry chromate, schematic illustration of formation of monodentate and bidentate complexes between MG-modified WL and $HCrO_4^-/CrO_4^{2-}$ ions is presented on Fig. S3.

The state of interaction/bonding at solutes/sorbent surface can be described by fitting experimental data with various adsorption isotherms (Markovski et al. 2014b). Analysis of adsorption data was performed by using various isotherm models, and statistical criteria used to evaluate the quality of model fitting of adsorption data. The Langmuir isotherm model is given by Eq. (2), while thermodynamic parameters for

studied ions were first estimated using the Gibbs free energy equation and the linearized van't Hoff equation (i.e., the van't Hoff plot) as follows (Liu et al. 2015):

$$q_e = (Kq_{\max}C_e)/(1 + KC_e) \quad (2)$$

$$\Delta G^o = -RTlnK_L \quad (3)$$

$$lnK_L = -\frac{\Delta H^o}{RT} + \frac{\Delta S^o}{R} \quad (4)$$

where C_e is the equilibrium concentration of ion at equilibrium (mol L^{-1}), q_e is the amount of ions adsorbed per weight unit of solid at equilibrium (mol g^{-1}), K and K_L are Langmuir constants related to sorption affinity in L mg^{-1}, and L mol^{-1}, respectively, and q_{max} is the maximum sorption capacity (mol g^{-1}), $\Delta G°$ (kJ mol^{-1}) is the change of free energy, $\Delta H°$ (kJ mol^{-1}) is the change of enthalpy, $\Delta S°$ (kJ mol^{-1}) is the change of entropy, T (K) is the absolute temperature, and R is the ideal gas constant (0.008314 kJ mol^{-1} K^{-1}). The values of non-linear Langmuir adsorption isotherm and thermodynamic parameters at 298, 308, and 318 K for Cd^{2+}, Ni^{2+}, $HCrO_4^-/CrO_4^{2-}$, and $H_2PO_4^-/HPO_4^{2-}$ ions' adsorption, using WL/MG and WL-γ-APS/MG adsorbents, are presented in Tables 2 and 3, and Fig. S4. Linear Langmuir adsorption isotherms, as well as values of q_e, K, and K_L are presented in Fig. S5 and Tables S2 and S3.

According to the Langmuir isotherm, mechanism of Cd^{2+}, Ni^{2+}, $HCrO_4^-/CrO_4^{2-}$, and phosphate ions' adsorption onto WL/MG and WL-γ-APS/MG sorbents can be described by monolayer adsorption with equal energy and enthalpy for all adsorption sites. Langmuir isotherm assumed that the energy of adsorption is generally considerably larger than for the second and higher layers, and therefore, multilayer formation is less possible (Rouquerol et al. 1999).

The results presented in Table 2 show high predicted adsorption capacity for both WL/MG and WL-γ-APS/MG adsorbents, and increase of adsorption capacity with the temperature increases. Moreover, adsorption results significantly support better adsorption performances of WL-γ-APS/MG (26.7–33.0% higher q_e) due to developed surface formed by size and distribution controllable deposition of MG on WL/DA.

The higher values of the Langmuir constant, which reflect the sorption affinity, were obtained for adsorption of all ions on WL-γ-APS/MG adsorbents at all temperatures. Higher temperature dependence was obtained for $H_2PO_4^-/HPO_4^{2-}$ and $HCrO_4^-/CrO_4^{2-}$ oxyanions, which means higher probability of surface complexation at higher temperature. Comparing obtained values of the Langmuir constant, it can be concluded that WL/MG and WL-γ-APS/MG adsorbents have higher sorption affinity for Ni^{2+} and Cd^{2+} as a result of their bonding mechanism. It can be explained by complex formation of monodentate mononuclear and bidentate binuclear complexes of $HCrO_4^-/CrO_4^{2-}$ and $H_2PO_4^-/HPO_4^{2-}$ ions with MG surface hydroxylic groups, while Ni^{2+} and Cd^{2+} ions easily create electrostatic interactions with MG centers. Moreover, the complexation of all investigated pollutant is easier with developed surface of W-γ-APS/MG adsorbent.

The negative $\Delta G°$ values indicate that adsorption occurs via spontaneous reactions (Veličković et al. 2012). Structure and stability of multilayered hydrated ions, charged or neutral, depend on the pH and temperature. Changes in pH value dictate the presence of ionic species which in turn affect structure/extent of interaction in hydration shell. Desolvation and diffusion at higher temperatures are more feasible processes, which are noticed as slight $\Delta G°$ increase with temperature increases. According to general rules, the change of $\Delta G°$ for physisorption lies between − 20 and 0 kJ mol^{-1}, both physisorption and chemisorption in the range from − 20 to − 80 kJ mol^{-1}, while the chemisorption is between − 80 and − 200 kJ mol^{-1}. Obtained results indicate contribution of both physisorption and chemisorption (Vuković et al. 2010, 2011; Budimirović et al. 2017).

The positive $\Delta H°$ also indicates the endothermic nature of adsorption for all studied ions (Liu et al. 2015) (Table 3). The $\Delta H°$ does not significantly vary between cation adsorption on WL/MG, while slightly increases for Cd^{2+} adsorption on WL-γ-APS/MG. The highest $\Delta H°$ values are obtained for WL-γ-APS/MG for oxyanions. Low endothermic nature reflects low energy released/consumed by desolvation of cation and formation of an M^{2+}/surface interactions, which could at appropriate balance. Higher $\Delta H°$ for oxyanions adsorption indicates higher energetic contribution of surface reaction and diffusional processes at lower extent. All of these contributing elementary processes are individually low to significant and could be either exothermic or endothermic, and their summary effect was found to be low endothermic.

The positive $\Delta S°$ relates to desolvation of structurally ordered hydronium ion and subsequent increase in randomness with increased concentration of adsorbed ions on the solid surface (Liu et al. 2015). Water molecules in surrounding solvation shell of metal ion form ordered structure, which after disruption of hydrogen-bonding increase system disorder. Positive values of entropy change ($\Delta S°$) indicate the increase in disorder (randomness) on boundary solid-liquid surface. The M^{2+}/surface interactions and oxyanion complex formation means decrease in translational, rotational, and vibrational motions which contributes to entropy decrease. Simultaneously, $\Delta S°$ increases due to both liberation of water due to adsorption and from cation hydration shell.

Except for this, results of reusability study showed low decrease of adsorption efficiency after three adsorptions/desorption cycles. An adsorption efficiency decrease of 22%, 20%, 25%, and 18% for Cd^{2+}, Ni^{2+}, $HCrO_4^-/CrO_4^{2-}$, and $H_2PO_4^-/HPO_4^{2-}$ ions, respectively, was obtained after the third adsorption/desorption cycle using WL/MG adsorbent. Hence, lower decrease of adsorption efficiency

Table 2 Nonlinear Langmuir isotherm parameters for Cd^{2+}, Ni^{2+},$H_2PO_4^-/HPO_4^{2-}$, and $HCrO_4^-/CrO_4^{2-}$ ions obtained at 298, 308, and 318 K using WL/MG and WL-γ-APS/MG adsorbents

	T (K)	q_e (mg g^{-1})	K (L mg^{-1})	R^2	q_e (mg g^{-1})	K (L mg^{-1})	R^2
	Cd^{2+}				Ni^{2+}		
WL/MG	298	50.543	24.313	0.960	47.889	23.330	0.936
	308	53.429	22.389	0.922	50.216	22.856	0.909
	318	55.450	25.867	0.969	52.019	26.911	0.969
WL-γ-APS/MG	298	69.289	19.096	0.876	61.412	24.638	0.989
	308	69.724	44.152	0.986	63.076	28.920	0.979
	318	73.126	61.886	0.986	66.144	37.083	0.988
	$H_2PO_4^-/HPO_4^{2-}$				$HCrO_4^-/CrO_4^{2-}$		
WL/MG	298	44.529	17.021	0.943	42.824	14.940	0.844
	308	46.262	19.060	0.947	44.447	13.262	0.808
	318	48.132	19.637	0.962	47.382	14.477	0.829
WL-γ-APS/MG	298	60.019	35.202	0.957	62.133	12.071	0.903
	308	62.702	35.921	0.981	63.632	19.354	0.917
	318	64.168	38.153	0.965	63.456	37.923	0.973

of 18%, 17%, 19%, and 13% for Cd^{2+}, Ni^{2+}, $HCrO_4^-/CrO_4^{2-}$, and $H_2PO_4^-/HPO_4^{2-}$ ions, respectively, was obtained after the third adsorption/desorption cycle using WL-γ-APS/MG adsorbent. According to this, it can be concluded that modification of WL-based ceramic (support) with magnetic iron-oxide form (magnetite) via γ-APS/DA cross-linker gave adsorbent with higher stability of MG deposit. Moreover, with proper selection of technology for the treatment of spent waste, alkali concentrated Cd^{2+}, Ni^{2+}, $HCrO_4^-/CrO_4^{2-}$, and $H_2PO_4^-/HPO_4^{2-}$ ions provide safe technology for their removal.

Competitive adsorption study of Cd^{2+}, Ni^{2+}, $HCrO_4^-/CrO_4^{2-}$, and $H_2PO_4^-/HPO_4^{2-}$ ions' removal from real water sample

Evaluation of WL/MG and WL-γ-APS/MG adsorbents' potential use for Cd^{2+}, Ni^{2+}, $HCrO_4^-/CrO_4^{2-}$, and $H_2PO_4^-/HPO_4^{2-}$ ions' removal from real water samples, contaminated natural water from the area of the city of Zrenjanin (located in Vojvodina, Serbia), was used for sorption experiment before any purification treatment. Other anions of interest present in water sample are SO_4^{2-} (42.5ppm) and Cl^- (1.2 ppm) (Taleb et al. 2016b). Kinetic experiments performed with 100 ppm of WL/MG and WL-γ-APS/MG adsorbents were carried out to find out the level of the efficiency of total Cd^{2+}, Ni^{2+}, $HCrO_4^-/CrO_4^{2-}$, and $H_2PO_4^-/HPO_4^{2-}$ ions' removal in natural water sample. It was found that competition of SO_4^{2-} and Cl^- ions was negligible (Petrova et al. 2011).

Adsorption kinetic study

Effect of time on pollutant adsorption was studied in a batch system containing m/V 125 mg L^{-1} of adsorbent at pH of 6.5 ± 0.10 for Cd^{2+} and Ni^{2+} and of 7.5 ± 0.10 for $HCrO_4^-/CrO_4^{2-}$ and $H_2PO_4^-/HPO_4^{2-}$ ions. The ions' concentration was determined after 5, 10, 15, 30, 60, and 90 min. In order to properly describe adsorption kinetic, the obtained experimental data was fitted using different kinetic rate equations (Bizerea Spiridon and Pitulice 2014). According to the highest values of correlation coefficient, R^2, which is a measure of conformity between experimental data and calculated ones, it was proved that pseudo-second-order (PSO), i.e., Eq. (5), was the most appropriate model for the description of kinetic processes for both WL/MG and WL-γ-APS/MG adsorbents (Tables 4 and S4 and Figs. S6 (linear) and S7 (nonlinear fit)):

$$\frac{dq_t}{dt} = k_2(q_e - q_t)^2 \tag{5}$$

The adsorption capacities at equilibrium and at time t (min) are defined by q_e and q_t (mg g^{-1}), respectively; k_2 is the PSO rate constant (g mg^{-1} min^{-1}). The kinetic parameters, presented in Table 4, showed that both sorbents, and preferentially WL-γ-APS/MG, possess high affinity with respect to studied ions and satisfactory rate at which system attains its equilibrium. According to pseudo-second-order kinetic law, the rate limiting step may be chemical adsorption involving valent forces through sharing or the exchange of electrons between the sorbents and divalent metal ions (Qiu et al. 2009). The analysis of kinetic data, using PSO kinetic method, resulted in significantly higher rate constant (1.17 to 13.4 times higher) and relatively balanced values of adsorption capacity of studied ions using WL-γ-APS/MG adsorbent at all temperatures. The k_2 values increase with increasing the temperature, and

Table 3 Thermodynamic parameters Cd^{2+}, Ni^{2+}, $H_2PO_4^-/HPO_4^{2-}$, and $HCrO_4^-/CrO_4^{2-}$ ions obtained at 298, 308, and 318 K using WL/MG and WL-γ-APS/MG adsorbents

	T (K)	$\Delta G°$ (kJ mol^{-1})	$\Delta H°$ (kJ mol^{-1})	$\Delta S°$ (J mol^{-1} K^{-1})	$\Delta G°$ (kJ mol^{-1})	$\Delta H°$ (kJ mol^{-1})	$\Delta S°$ (J mol^{-1} K^{-1})
		Cd^{2+}			Ni^{2+}		
WL/MG	298	− 45.23	2.15	159.10	− 45.20	2.01	158.75
	308	− 47.01			− 47.01		
	318	− 48.40			− 48.36		
WL-γ-APS/MG	298	− 46.21	12.64	198.04	− 45.19	9.32	183.33
	308	− 48.80			− 47.48		
	318	− 50.14			− 48.83		
		$H_2PO_4^-/HPO_4^{2-}$			$HCrO_4^-/CrO_4^{2-}$		
WL/MG	298	− 39.61	8.69	161.88	− 41.34	5.36	156.65
	308	− 41.11			− 42.92		
	318	− 42.86			− 44.48		
WL-γ-APS/MG	298	− 40.09	29.10	231.46	− 40.69	21.50	208.95
	308	− 41.89			− 43.13		
	318	− 44.79			− 44.85		

the highest values are obtained at 318 K. These results indicate more efficient diffusional transport/adsorbate complexation at adsorbent surface versus temperature increase. Determination of activation parameters could give information on both energetic requirements to overcome slowest adsorption step and adsorption mechanism. The energy of activation (E_a) was calculated from the linear plot of the values of logarithms of rate constants (k_2) versus $1/T$ obtained by linearization of Arrhenius equation (Eq. (6)) (results obtained in kinetic study at 298 K using the Eq. (5) (March 1985)):

$$k_2 = Ae^{-(E_a/RT)} \tag{6}$$

Adsorption kinetics is generally controlled by diffusive mass transfer; thus, rates of approaching to equilibrium usually increases with increasing of the temperature. For the cations' adsorption on both adsorbents, the results show that the intra-particle diffusion is a rate-controlling step since the activation energy is low and within the range of 6–17.5 kJ mol^{-1} characteristic for diffusion-controlled processes (Haring 1942). The higher activation energies for the adsorption of oxyanions reflect significance of morphological/porosity factor to improved adsorption kinetic.

The kinetic data results (Table S5) obtained by applying Weber–Morris (W-M) kinetic model were useful in the evaluation of rate limiting step of overall process (Vuković et al. 2011). High values of W-M constant C_1 for both cations and oxyanions (Table S5) indicate that intra-particle diffusion is not the only rate limiting step; complex influence of the other factors determines the effectiveness of overall pollutant transport. At the initial stage of the process, the diffusion from bulk phase to the exterior surface takes place at high rate, while second linear part, which depends on material porosity, relates to the diffusion inside mesopores/micropores.

Various adsorbents for Cd^{2+}, Ni^{2+}, $HCrO_4^-/CrO_4^{2-}$, and $H_2PO_4^-/HPO_4^{2-}$ ions' removal, including unmodified and iron-oxide modified materials such as activated carbon, clays, cellulose-based materials, and WL-based sorbents, were reported in literature (Vuković et al. 2010; Karnib et al. 2014; Taleb et al. 2016b). Cd^{2+}, Ni^{2+}, $HCrO_4^-/CrO_4^{2-}$, and $H_2PO_4^-/HPO_4^{2-}$ ions' adsorption capacities (value of q_e derived from Langmuir equation) of various WL and magnetite-based adsorbents are summarized in Table S6. According to the presented Cd^{2+}, Ni^{2+}, $HCrO_4^-/CrO_4^{2-}$, and $H_2PO_4^-/HPO_4^{2-}$ ions' adsorption capacities on WL and MG-based adsorbents, with regard to other equilibrium contact times, the applied adsorbent in the present study could potentially be used as efficient adsorbent to remove Cd^{2+}, Ni^{2+}, $HCrO_4^-/CrO_4^{2-}$, and $H_2PO_4^-/HPO_4^{2-}$ ions from aqueous solutions in a short time period. Both, bare WL and MG nanoparticles, showed moderate adsorption capacities (6.5–13.5 mg g^{-1}) for Cd^{2+}, Ni^{2+}, $HCrO_4^-/CrO_4^{2-}$, and $H_2PO_4^-/HPO_4^{2-}$ ions' removal. Moreover, hybrid adsorbents obtained by MG precipitation on porous WL support showed higher adsorption capacities (52.41–73.15 mg g^{-1}) due to availability of more active sites for heavy metals' removal and oxyions complexation.

Monolayer model for single-compound adsorption

For the monolayer model for single-compound adsorption, it is assumed that heavy metal ions/oxyanions are adsorbed with one energy ($-\varepsilon$) (Sellaoui et al. 2017a). The $-\varepsilon$ describes the interaction of ions with the surface of the MG-modified WL-based sorbents. Adsorption

Table 4 Kinetic and activation parameters obtained by the use of nonlinear PSO kinetic model for the Cd^{2+}, Ni^{2+}, $HCrO_4^-/CrO_4^{2-}$, and $H_2PO_4^-/HPO_4^{2-}$ removal using WL/MG and WL-γ-APS/MG adsorbents

298 K			
	Pseudo-second-order	Cd^{2+}	Ni^{2+}
WL/MG	$k_2 \times 10^2$ (g mg^{-1} min^{-1})	0.193 ± 0.029	0.208 ± 0.009
	q_e (mg g^{-1})	55.878 ± 1.003	54.618 ± 1.125
	R^2	0.960	0.973
	Ea (kJ mol^{-1})	11.43	17.38
WL-γ-APS/MG	$k_2 \times 10^2$ (g mg^{-1} min^{-1})	1.222 ± 0.021	1.187 ± 0.005
	q_e (mg g^{-1})	70.027 ± 1.112	62.563 ± 1.082
	R^2	0.992	0.991
	Ea (kJ mol^{-1})	20.78	24.20
	Pseudo-second-order	$H_2PO_4^-/HPO_4^{2-}$	$HCrO_4^-/CrO_4^{2-}$
WL/MG	$k_2 \times 10^2$ (g mg^{-1} min^{-1})	0.594 ± 0.012	0.248 ± 0.017
	q_e (mg g^{-1})	42.819 ± 1.124	46.982 ± 1.115
	R^2	0.927	0.972
	Ea (kJ mol^{-1})	13.91	27.12
WL-γ-APS/MG	$k_2 \times 10^2$ (g mg^{-1} min^{-1})	1.018 ± 0.010	1.215 ± 0.020
	q_e (mg g^{-1})	60.638 ± 0.719	59.574 ± 1.108
	R^2	0.947	0.952
	Ea (kJ mol^{-1})	28.92	25.02
	308 K		
	Pseudo-second-order	Cd^{2+}	Ni^{2+}
WL/MG	$k_2 \times 10^2$ (g mg^{-1} min^{-1})	0.223 ± 0.012	0.238 ± 0.001
	q_e (mg g^{-1})	59.445 ± 0.748	58.931 ± 1.197
	R^2	0.988	0.975
WL-γ-APS/MG	$k_2 \times 10^2$ (g mg^{-1} min^{-1})	2.075 ± 0.007	2.030 ± 0.007
	q_e (mg g^{-1})	69.883 ± 1.221	62.411 ± 1.223
	R^2	0.999	0.998
	Pseudo-second-order	$H_2PO_4^-/HPO_4^{2-}$	$HCrO_4^-/CrO_4^{2-}$
WL/MG	$k_2 \times 10^2$ (g mg^{-1} min^{-1})	0.785 ± 0.003	0.282 ± 0.001
	q_e (mg g^{-1})	45.300 ± 1.022	47.734 ± 1.690
	R^2	0.994	0.995
WL-γ-APS/MG	$k_2 \times 10^2$ (g mg^{-1} min^{-1})	2.452 ± 0.008	2.402 ± 0.003
	q_e (mg g^{-1})	61.336 ± 1.103	62.494 ± 0.426
	R^2	0.973	0.947
	318 K		
	Pseudo-second-order	Cd^{2+}	Ni^{2+}
WL/MG	$k_2 \times 10^2$ (g mg^{-1} min^{-1})	0.258 ± 0.007	0.324 ± 0.001
	q_e (mg g^{-1})	54.621 ± 2.686	55.410 ± 1.303
	R^2	0.997	0.986
WL-γ-APS/MG	$k_2 \times 10^2$ (g mg^{-1} min^{-1})	2.068 ± 0.002	2.183 ± 0.008
	q_e (mg g^{-1})	73.092 ± 0.299	65.730 ± 0.987
	R^2	0.992	0.979
	Pseudo-second-order	$H_2PO_4^-/HPO_4^{2-}$	$HCrO_4^-/CrO_4^{2-}$
WL/MG	$k_2 \times 10^2$ (g mg^{-1} min^{-1})	0.851 ± 0.004	0.496 ± 0.001
	q_e (mg g^{-1})	46.939 ± 1.001	47.402 ± 1.112
	R^2	0.966	0.939
WL-γ-APS/MG	$k_2 \times 10^2$ (g mg^{-1} min^{-1})	2.097 ± 0.004	2.332 ± 0.004
	q_e (mg g^{-1})	63.999 ± 0.682	63.184 ± 0.636
	R^2	0.899	0.993

energy is calculated according to the following equation (Sellaoui et al. 2017b):

$$\varepsilon = k_B T \ln\left(\frac{c_s}{c_{1/2}}\right) \quad (7)$$

where k_B is the Boltzmann constant, c_s is the solubility of the heavy metal, and $c_{1/2}$ is the concentration at half saturation (Sellaoui et al. 2016a, b). According to the general Langmuir model interpretation, each adsorption site accommodates one ion, as following chemical pseudo-reactions describe (Sellaoui et al. 2017a, b):

$$n\mathrm{A}^{2+} + \mathrm{S} \leftrightarrow \mathrm{A}^{2+}n\mathrm{S} \quad (8)$$

$$n\mathrm{B}^{-} + \mathrm{S} \leftrightarrow \mathrm{B}^{-}n\mathrm{S} \quad (9)$$

$$n\mathrm{B}^{2-} + \mathrm{S} \leftrightarrow \mathrm{B}^{2-}n\mathrm{S} \quad (10)$$

where A^{2+} represents the adsorbed Cd^{2+} or Ni^{2+} ions, S is the adsorbent receptor site, $A^{2+}nS$ represents formed complex of cations with MG-modified WL-based sorbents, n represents number of the bonded ions per one receptor site, B^{-} and B^{2-} represent the mono- and divalent chromate or phosphate oxyanions, and B^{-} nS and B^{2-} nS represent formed complexes of oxyanions with MG-modified WL-based sorbents. The partition function of one identical site and the monolayer model for single-compound adsorption are described by the following equations:

$$Z_{gc} = 1 + e^{\beta(\varepsilon+\mu)} \quad (11)$$

$$Z_{gc} = e^{\beta(\varepsilon+\mu)N_M} \quad (12)$$

$$Q = \frac{nN_M}{1 + \left(\frac{c_{1/2}}{c}\right)^n} \quad (13)$$

In these expressions, ε represents the adsorption energy of the receptor site, μ is the chemical potential of the adsorbed state determined from the Gibbs free energy, β is the Boltzmann factor, defined as $1/(k_B T)$, Q is the adsorption capacity, n is the number of ions per site, N_M is the density of receptor site, and c is the heavy metal ion/oxyanion equilibrium concentration (Sellaoui et al. 2016a, b). Different values for the parameters for single-compound adsorption of heavy metal ions/oxyanions on MG-modified WL-based sorbents are presented in Table 5.

The determination of the number of ions that interact with one receptor site offers reliable information complementing the conclusions for adsorption phenomena obtained from the isothermal adsorption study. If the number of the bonded/complexed ions/oxyanions per site is lower than 1, the ions interact with at least two receptor sites (multi-link). On the opposite, if the n is higher than 1, the receptor site is occupied minimum by one ion (Sellaoui et al. 2017a, b). For all of the investigated single-compound systems (adsorption of Cd^{2+}, Ni^{2+}, $HCrO_4^{-}/CrO_4^{2-}$, and $H_2PO_4^{-}/HPO_4^{2-}$ on WL-based adsorbents), the lowest values of the n are obtained at 298 K. It confirms that the main mechanism of the Cd^{2+} and Ni^{2+} ions' adsorption occurs via exchange of metal ions Cd^{2+}/Ni^{2+} with H^{+} ions at the surface hydroxyl groups –FeOH (receptor site) producing $Cd^{2+}/Ni^{2+}(OH)^{+}$ ions that are bonded with another

Table 5 Values of adjustable parameters in single-compound system for the adsorption of Cd^{2+}, Ni^{2+}, $HCrO_4^{-}/CrO_4^{2-}$, and $H_2PO_4^{-}/HPO_4^{2-}$ ions

	T (K)	ε (KJ mol^{-1})	Q_{sat} (mg g^{-1})	N_M (mg g^{-1})	n	ε (KJ mol^{-1})	Q_{sat} (mg g^{-1})	N_M (mg g^{-1})	n
		Cd^{2+}				Ni^{2+}			
WL/MG	298	7.624	55.878	45	0.66	6.781	54.618	44	1.21
	308	7.967	59.445	45	0.85	7.108	58.931	44	0.91
	318	7.388	54.621	45	1.11	7.411	55.410	44	0.88
WL-γ-APS/MG	298	7.698	70.027	45	0.82	6.822	62.563	44	0.70
	308	8.024	69.883	43	0.96	7.126	62.411	43	0.99
	318	8.491	73.092	43	1.21	8.388	65.730	44	1.25
		$HCrO_4^{-}/CrO_4^{2-}$				$H_2PO_4^{-}/HPO_4^{2-}$			
WL/MG	298	6.310	46.982	49	0.65	6.059	42.819	53	0.58
	308	6.715	47.734	49	0.66	6.364	45.300	53	0.59
	318	7.097	47.402	49	0.73	8.649	46.939	52	0.59
WL-γ-APS/MG	298	6.397	59.574	50	0.57	6.181	60.638	52	0.67
	308	6.364	62.494	48	0.57	6.479	61.336	55	0.68
	318	6.650	63.184	48	0.59	6.779	63.999	50	0.69

MG-modified WL receptor site. Also, electrostatic interactions of ion positive charge with electron pair of hydroxyl groups could be of appropriate significance. By changing the adsorption operational conditions (increasing temperature), the values of the *n* increase as well. For the Cd^{2+} ions' adsorption on both WL-MG and WL-γ-APS/MG adsorbents, the highest values of *n* (higher than 1) are obtained at 318 K. This indicates appropriate change of metal binding mechanism, i.e., higher number of ions per one site, with concomitant increase of adsorption capacity (Table 2). Opposite is found for Ni^{2+} ions' adsorption on WL-MG adsorbent where the highest values of *n* are obtained at 298 K. Lower values of *n* parameters are found for the $HCrO_4^-/CrO_4^{2-}$ and $H_2PO_4^-/HPO_4^{2-}$ ions (Table 5) indicating different adsorption mechanisms in relation to cations. The *n* values in the range 0.57–0.73 for $HCrO_4^-/CrO_4^{2-}$ and 0.59–0.69 for $H_2PO_4^-/HPO_4^{2-}$ indicate that main mechanism represents interaction one ion per two active surface sites which is in good accordance with the creation of bidentate mononuclear and binuclear surface complexes of both ions (Zach-Maor et al. 2011; Johnston and Chrysochoou 2014). The parameter *n* also increases with temperature increase.

Conclusion

Magnetite-modified porous wollastonite-based ceramics were synthesized using ultra-fine PMMA as a pore-forming agent in order to obtain hybrid adsorbents with high adsorption performances for heavy metals and oxyanions. FTIR, Raman, XRD, and Mössbauer measurements confirmed wollastonite and larnite phases at pure WL support and successfulness of magnetite precipitation. SEM analysis confirmed macro- and microporosity of pure WL support and formation of MG aggregates on WL. Synthesized MG-modified WL-based sorbent was used for Cd^{2+}, Ni^{2+}, $HCrO_4^-/CrO_4^{2-}$, and $H_2PO_4^-/HPO_4^{2-}$ ions' removal. Results showed that pH is an important parameter that controls the effectiveness of pollutant removal.

The quality of the isotherm modeling of adsorption data was estimated by the correlation coefficients. The best adsorption model was found to be the Langmuir isotherm. The kinetic data of the sorption were well fitted with the pseudo-second-order kinetic model. A significantly higher second-order rate constant of Cd^{2+}, Ni^{2+}, $HCrO_4^-/CrO_4^{2-}$, and $H_2PO_4^-/HPO_4^{2-}$ ions' adsorption was obtained using WL-γ-APS/MG as adsorbent. Higher activation energies were obtained for oxyanion adsorption.

Statistical physic theory was used for the interpretation of single adsorption isotherm and adsorption phenomena. The absorption parameters in a single-compound system deducted by the monolayer model with one energy confirmed that the adsorption of Cd^{2+} and Ni^{2+} ions occurred via mostly one ion with two receptor sites' interactions. For the $HCrO_4^-/CrO_4^{2-}$ and $H_2PO_4^-/HPO_4^{2-}$ ions' adsorption, the statistical physic model confirmed that multiple adsorption mechanisms electrostatic interaction/complexation occurred.

Acknowledgement The authors are grateful to Dr. Miodrag Mitrić for XRD measurements.

Funding information This research was performed within the projects OI 172057, OI 171001, and 176018, funded by the Ministry of Education, Science and Technological Development of the Republic of Serbia, and bilateral cooperation between Serbia and France, No. 4510339/2016/09/03 "Inteligent eco-nanomaterials and nanocomposites." The work was supported in part by the National Science Foundation, North Carolina State University (Project No. HRD-1345219 and DMR-1523617) and the National Aeronautics and Space Administration project (NASA: NNX09AV07A).

References

Abdel-Halim ES, Al-Deyab SS (2011) Removal of heavy metals from their aqueous solutions through adsorption onto natural polymers. Carbohydr Polym 84:454–458. https://doi.org/10.1016/j.carbpol.2010.12.001

Ahmed MA, Ali SM, El-Dek SI, Galal A (2013) Magnetite–hematite nanoparticles prepared by green methods for heavy metal ions removal from water. Mater Sci Eng B 178:744–751. https://doi.org/10.1016/j.mseb.2013.03.011

Bizerea Spiridon O, Preda E, Botez A, Pitulice L (2014) Phenol removal from wastewater by adsorption on zeolitic composite. Environ Sci Pollut Res 20:6367–6381. https://doi.org/10.1007/s11356-013-1625-x

Boehm HP (1994) Some aspects of the surface chemistry of carbon blacks and other carbons. Carbon 32:759–769

Brand R (2008) WinNormos Mössbauer fitting program

Budimirović D, Veličković ZS, Djokić VR, Milosavljević M, Markovski J, Lević S, Marinković AD (2017) Efficient As(V) removal by α-FeOOH and α-FeOOH/ α-MnO_2 embedded PEG-6-arm functionalized multiwall carbon nanotubes. Chem Eng Res Des 119:75–86. https://doi.org/10.1016/j.cherd.2017.01.010

Buzatu A, Buzgar N (2010) The Raman study of single-chain silicates. Analele Stiint ale Univ "Al I Cuza" din Iasi , Geol 56:107–125. https://doi.org/10.13140/2.1.4600.9288

Capretta A, Maharajh RB, Bell RA (1995) Synthesis and characterization of cyclomaltoheptaose-based metal chelants as probes for intestinal permeability. Carbohydr Res 267:49–63. https://doi.org/10.1016/0008-6215(94)00289-R

Carvalho MD, Henriques F, Ferreira LP, Godinho M, Cruz MM (2013) Iron oxide nanoparticles: the influence of synthesis method and size on composition and magnetic properties. J Solid State Chem 201:144–152. https://doi.org/10.1016/j.jssc.2013.02.024

Chen Q, Hills CD, Yuan M, Liu H, Tyrer M (2008) Characterization of carbonated tricalcium silicate and its sorption capacity for heavy metals: a micron-scale composite adsorbent of active silicate gel and calcite. J Hazard Mater 153:775–783. https://doi.org/10.1016/j.jhazmat.2007.09.023

da Costa GM, De Grave E, Vandenberghe RE (1998) Mössbauer studies of magnetite and Al-substituted maghemites. Hyperfine Interact 117:207–243. https://doi.org/10.1023/A:1012691209853

D'Halluin M, Rull-Barrull J, Bretel G et al (2017) Chemically modified cellulose filter paper for heavy metal remediation in water. ACS

Sustain Chem Eng 5:1965–1973. https://doi.org/10.1021/acssuschemeng.6b02768

da Costa GM (1995) Influence of nonstoichiometry and the presence of maghemite on the Mössbauer spectrum of magnetite†. Clay Clay Miner 43:656–668. https://doi.org/10.1346/CCMN.1995.0430602

de Faria DLA, Venâncio Silva S, de Oliveira MT (1997) Raman microspectroscopy of some iron oxides and oxyhydroxides. J Raman Spectrosc 28:873–878. https://doi.org/10.1002/(SICI)1097-4555(199711)28:11<873::AID-JRS177>3.0.CO;2-B

Dézsi I, Fetzer C, Gombkötő Á, Szűcs I, Gubicza J, Ungár T (2008) Phase transition in nanomagnetite. J Appl Phys 103:104312. https://doi.org/10.1063/1.2937252

Ding H, Lu SC, Du GX (2011) Surface modification of wollastonite by the mechano-activated method and its properties. Int J Miner Metall Mater 18:83–88. https://doi.org/10.1007/s12613-011-0404-2

Dowty E, Lindsley DH (1973) Mössbauer spectra of synthetic Ca-Fe pyroxenoids and lunar pyroxferroite. Contrib Mineral Petrol 48: 229–232. https://doi.org/10.1007/BF00383358

Drah A, Tomić NZ, Veličić Z, Marinković AD, Radovanović Ž, Veličković Z, Jančić-Heinemann R (2017) Highly ordered macroporous γ -alumina prepared by a modified sol-gel method with a PMMA microsphere template for enhanced Pb^{2+}, Ni^{2+} and Cd^{2+} removal. Ceram Int 43:13817–13827. https://doi.org/10.1016/j.ceramint.2017.07.102

Dyar MD, Agresti DG, Schaefer MW, Grant CA, Sklute EC (2006) Mössbauer spectroscopy of Earth and planetary materials. Annu Rev Earth Planet Sci 34:83–125. https://doi.org/10.1146/annurev.earth.34.031405.125049

Ebbert C, Grundmeier G, Buitkamp N, Kröger A, Messerschmidt F, Thissen P (2014) Toward a microscopic understanding of the calcium–silicate–hydrates/water interface. Appl Surf Sci 290:207–214. https://doi.org/10.1016/j.apsusc.2013.11.045

EPA (2014) United State Environmental Protection Agency

Fock J, Bogart LK, González-Alonso D, Espeso JI, Hansen MF, Varón M, Frandsen C, Pankhurst QA (2017) On the 'centre of gravity' method for measuring the composition of magnetite/maghemite mixtures, or the stoichiometry of magnetite-maghemite solid solutions, via ^{57}Fe Mössbauer spectroscopy. J Phys D Appl Phys 50:265005. https://doi.org/10.1088/1361-6463/aa73fa

Gorski CA, Scherer MM (2010) Determination of nanoparticulate magnetite stoichiometry by Mössbauer spectroscopy, acidic dissolution, and powder X-ray diffraction: a critical review. Am Mineral 95: 1017–1026. https://doi.org/10.2138/am.2010.3435

Gustafsson JP (2011) Visual MINTEQ. 3.0, beta

Han Q, Chen L, Li W, Zhou Z, Fang Z, Xu Z, Qian X (2018) Self-assembled three-dimensional double network graphene oxide/polyacrylic acid hybrid aerogel for removal of Cu^{2+} from aqueous solution. Environ Sci Pollut Res 25:34438–34447. https://doi.org/10.1007/s11356-018-3409-9

Haring MM (1942) The theory of rate processes (Glasstone, Samuel; Laidler, Keith J.; Eyring, Henry). J Chem Educ 19:249 19:249. https://doi.org/10.1021/ed019p249.1

Huang X, Zhan X, Wen C, Xu F, Luo L (2017) Amino-functionalized magnetic bacterial cellulose/activated carbon composite for Pb^{2+} and methyl orange sorption from aqueous solution. J Mater Sci Technol 34:855–863. https://doi.org/10.1016/j.jmst.2017.03.013

Iannazzo D, Pistone A, Ziccarelli I, Espro C, Galvagno S, Giofré SV, Romeo R, Cicero N, Bua GD, Lanza G, Legnani L, Chiacchio MA (2017) Removal of heavy metal ions from wastewaters using dendrimer-functionalized multi-walled carbon nanotubes. Environ Sci Pollut Res 24:14735–14747. https://doi.org/10.1007/s11356-017-9086-2

Johnston CP, Chrysochoou M (2014) Mechanisms of chromate adsorption on hematite. Geochim Cosmochim Acta 138:146–175

Joos A, Rümenapp C, Wagner FE, Gleich B (2016) Characterisation of iron oxide nanoparticles by Mössbauer spectroscopy at ambient temperature. J Magn Magn Mater 399:123–129. https://doi.org/10.1016/j.jmmm.2015.09.060

Kalantari K, Ahmad MB, Masoumi HRF, Shameli K, Basri M, Khandanlou R (2014) Rapid adsorption of heavy metals by Fe_3O_4/talc nanocomposite and optimization study using response surface methodology. Int J Mol Sci 15:12913–12927. https://doi.org/10.3390/ijms150712913

Kalska-Szostko B, Satuła D, Olszewski W (2015) Mössbauer spectroscopy studies of the magnetic properties of ferrite nanoparticles. Curr Appl Phys 15:226–231. https://doi.org/10.1016/j.cap.2014.12.011

Karnib M, Kabbani A, Holail H, Olama Z (2014) Heavy metals removal using activated carbon, silica and silica activated carbon composite. Energy Procedia 50:113–120. https://doi.org/10.1016/j.egypro.2014.06.014

Karthikeyan T, Rajgopal S, Miranda LR (2005) Chromium(VI) adsorption from aqueous solution by Hevea brasiliensis sawdust activated carbon. J Hazard Mater 124:192–199. https://doi.org/10.1016/j.jhazmat.2005.05.003

Khalil MI (2015) Co-precipitation in aqueous solution synthesis of magnetite nanoparticles using iron(III) salts as precursors. Arab J Chem 8:279–284. https://doi.org/10.1016/j.arabjc.2015.02.008

Kumari M, Pittman CU, Mohan D (2015) Heavy metals [chromium(VI) and lead(II)] removal from water using mesoporous magnetite (Fe_3O_4) nanospheres. J Colloid Interface Sci 442:120–132. https://doi.org/10.1016/j.jcis.2014.09.012

Kündig W, Steven Hargrove R (1969) Electron hopping in magnetite. Solid State Commun 7:223–227. https://doi.org/10.1016/0038-1098(69)90729-7

Li Y-S, Church JS, Woodhead AL (2012) Infrared and Raman spectroscopic studies on iron oxide magnetic nano-particles and their surface modifications. J Magn Magn Mater 324:1543–1550. https://doi.org/10.1016/j.jmmm.2011.11.065

Lin S, Lian C, Xu M, Zhang W, Liu L, Lin K (2017) Study on competitive adsorption mechanism among oxyacid-type heavy metals in co-existing system: removal of aqueous As(V), Cr(III) and As (III) using magnetic iron oxide nanoparticles (MIONPs) as adsorbents. Appl Surf Sci 422:675–681. https://doi.org/10.1016/j.apsusc.2017.06.079

Liu C-H, Chuang Y-H, Chen T-Y, Tian Y, Li H, Wang MK, Zhang W (2015) Mechanism of arsenic adsorption on magnetite nanoparticles from water: thermodynamic and spectroscopic studies. Environ Sci Technol 49:7726–7734. https://doi.org/10.1021/acs.est.5b00381

March J (1985) Advanced organic chemistry: reaction, mechanisms and structure. Wiley, New York

Markovski JS, Đokić V, Milosavljević M, Mitrić M, Perić-Grujić AA, Onjia AE, Marinković AD (2014a) Ultrasonic assisted arsenate adsorption on solvothermally synthesized calcite modified by goethite, α-MnO_2 and goethite/α-MnO_2. Ultrason Sonochem 21:790–801. https://doi.org/10.1016/j.ultsonch.2013.10.006

Markovski JS, Marković DD, Dokić VR et al (2014b) Arsenate adsorption on waste eggshell modified by goethite, α-MnO_2 and goethite/α-MnO_2. Chem Eng J 237:430–442. https://doi.org/10.1016/j.cej.2013.10.031

Martin S, Griswold W (2009) Human health effects of heavy metals. Cent Hazard Subst Res Enviromental Sci Technol Briefs Citizens:1–6

Mezenner NY, Bensmaili A (2009) Kinetics and thermodynamic study of phosphate adsorption on iron hydroxide-eggshell waste. Chem Eng J 147:87–96. https://doi.org/10.1016/j.cej.2008.06.024

Murad E, Wagner U (1998) Clays and clay minerals: the firing process. Hyperfine Interact 117:337–356. https://doi.org/10.1023/A:1012683008035

Obradović N, Filipović S, Marković S, Mitrić M, Rusmirović J, Marinković A, Antić V, Pavlović V (2017a) Influence of different pore-forming agents on wollastonite microstructures and adsorption capacities. Ceram Int 43:7461–7468. https://doi.org/10.1016/j.ceramint.2017.03.021

Obradović N, Filipović S, Rusmirović J et al (2017b) Formation of porous wollastonite-based ceramics after sintering with yeast as the pore-forming agent. Sci Sinter 49:49–246. https://doi.org/10.2298/SOS1703235O

Oshtrakh MI, Ushakov MV, Šepelák V, Semionkin VA, Morais PC (2016) Study of iron oxide nanoparticles using Mössbauer spectroscopy with a high velocity resolution. Spectrochim Acta Part A Mol Biomol Spectrosc 152:666–679. https://doi.org/10.1016/j.saa.2015.06.017

Osticioli I, Mendes NFC, Nevin A, Gil FPSC, Becucci M, Castellucci E (2009) Analysis of natural and artificial ultramarine blue pigments using laser induced breakdown and pulsed Raman spectroscopy, statistical analysis and light microscopy. Spectrochim Acta Part A Mol Biomol Spectrosc 73:525–531. https://doi.org/10.1016/j.saa.2008.11.028

Ovsyannikov SV, Shchennikov VV, Shvetsova MA, Dubrovinsky LS, Polian A (2010) Tuning of the stoichiometry of of $Fe_{1-x}O$ wüstite by compression wüstite by compression. Phys Rev B 81:060101. https://doi.org/10.1103/PhysRevB.81.060101

Paul D (2017) Research on heavy metal pollution of river Ganga: a review. Ann Agrar Sci 15:278–286. https://doi.org/10.1016/j.aasci.2017.04.001

Petrova TM, Fachikov L, Hristov J (2011) The magnetite as adsorbent for some hazardous species from aqueous solution: a review. Int Rev Chem Eng Int Rev Chem Eng 3:134–152

Qi Z, Joshi TP, Liu R, Liu H, Qu J (2017) Synthesis of Ce(III)-doped Fe_3O_4 magnetic particles for efficient removal of antimony from aqueous solution. J Hazard Mater 329:193–204. https://doi.org/10.1016/j.jhazmat.2017.01.007

Qiu H, Lv L, Pan B, Zhang QJ, Zhang WM, Zhang QX (2009) Critical review in adsorption kinetic models. J Zhejiang Univ Sci A 10:716–724. https://doi.org/10.1631/jzus.A0820524

Rajput S, Pittman CU, Mohan D (2016) Magnetic magnetite (Fe_3O_4) nanoparticle synthesis and applications for lead (Pb^{2+}) and chromium (Cr^{6+}) removal from water. J Colloid Interface Sci 468:334–346. https://doi.org/10.1016/j.jcis.2015.12.008

Razzaque MS (2011) Phosphate toxicity: new insights into an old problem. Clin Sci 120:91–97. https://doi.org/10.1042/CS20100377

Ricciardi P, Colomban P, Tournié A, Milande V (2009) Nondestructive on-site identification of ancient glasses: genuine artefacts, embellished pieces or forgeries? J Raman Spectrosc 40:604–617. https://doi.org/10.1002/jrs.2165

Richet P, Mysen BO, Ingrin J (1998) High-temperature X-ray diffraction and Raman spectroscopy of diopside and pseudowollastonite. Phys Chem Miner 25:401–414. https://doi.org/10.1007/s002690050130

Roggwiller P, Kundig W (1973) Mössbauer spectra of superparamagnetic Fe_3O_4. Differentiation 12:901–903

Rouquerol F, Rouquerol J, Sing K (1999) Adsorption by powders and porous solids: principles, methodology and application. Academic Press, USA

Rout PR, Bhunia P, Dash RR (2015) Effective utilization of a sponge iron industry by-product for phosphate removal from aqueous solution: a statistical and kinetic modelling approach. J Taiwan Inst Chem Eng 46:98–108. https://doi.org/10.1016/j.jtice.2014.09.006

Rout PR, Dash RR, Bhunia P (2016) Nutrient removal from binary aqueous phase by dolochar: highlighting optimization, single and binary adsorption isotherms and nutrient release. Process Saf Environ Prot 100:91–107. https://doi.org/10.1016/j.psep.2016.01.001

Sarin VK, Kent SBH, Tam JP, Merrifield RB (1981) Quantitative monitoring of solid-phase peptide synthesis by the ninhydrin reaction. Anal Biochem 117:147–157. https://doi.org/10.1016/0003-2697(81)90704-1

Sellaoui L, Bouzid M, Duclaux L, Reinert L, Knani S, Ben Lamine A (2016a) Binary adsorption isotherms of two ionic liquids and ibuprofen on an activated carbon cloth: simulation and interpretations using a statistical and COSMO-RS models. RSC Adv 6:67701–67714. https://doi.org/10.1039/C6RA03405E

Sellaoui L, Dotto GL, Ben LA, Erto A (2017a) Interpretation of single and competitive adsorption of cadmium and zinc on activated carbon using monolayer and exclusive extended monolayer models. Environ Sci Pollut Res 24:19902–19908. https://doi.org/10.1007/s11356-017-9562-8

Sellaoui L, Dotto GL, Goncalves JO et al (2016b) Equilibrium modeling of single and binary adsorption of Food Yellow 4 and Food Blue 2 on modified chitosan using a statistical physics theory: new microscopic interpretations. J Mol Liq 222:151–158. https://doi.org/10.1016/j.molliq.2016.07.005

Sellaoui L, Edi Soetaredjo F, Ismadji S, Cláudio Lima É, Dotto GL, Ben Lamine A, Erto A (2017b) New insights into single-compound and binary adsorption of copper and lead ions on treated sea mango shell: experimental and theoretical studies. Phys Chem Chem Phys 19:25927–25937. https://doi.org/10.1039/c7cp03770h

Sharma YC (2001) Adsorption of Cr(VI) onto wollastonite: effect of pH. Indian J Chem Technol 8:186–190

Sharma YC, Gupta GS, Prasad G, Rupainwar DC (1990a) Use of wollastonite in the removal of Ni(II) from aqueous solutions. Water Air Soil Pollut 49:69–79. https://doi.org/10.1007/BF00279511

Sharma YC, Prasad G, Rupainwar DI (1990b) Adsorption for removal of Cd(II) from effluents. Int J Environ Stud 36:315–320. https://doi.org/10.1080/00207239008710609

Sharma YC, Uma SV et al (2007) Reclamation of Cr(VI) rich water and wastewater by wollastonite. Chem Eng J 127:151–156. https://doi.org/10.1016/j.cej.2006.09.012

Shim SE, Kim K, Oh S, Choe S (2004) Preparation of ultra fine poly(methyl methacrylate) microspheres in methanol-enriched aqueous medium. Macromol Res 12:240–245. https://doi.org/10.1007/BF03218394

Sokol EV, Seryotkin YV, Kokh SN, Vapnik Y, Nigmatulina EN, Goryainov SV, Belogub EV, Sharygin VV (2015) Flamite, $(Ca,Na,K)_2(Si,P)O_4$, a new mineral from ultrahightemperature combustion metamorphic rocks, Hatrurim Basin, Negev Desert, Israel. Mineral Mag 79:583–596. https://doi.org/10.1180/minmag.2015.079.3.05

Sreekanth Chakradhar RP, Nagabhushana BM, Chandrappa GT, Ramesh KP, Rao JL (2006) Solution combustion derived nanocrystalline macroporous wollastonite ceramics. Mater Chem Phys 95:169–175. https://doi.org/10.1016/j.matchemphys.2005.06.002

Stevens JG, Khasanov AM, Miller JW et al (2005) Mössbauer mineral handbook. The University of North Carolina at Asheville

Suzdalev IP, Maksimov YV, Buravtsev VN, Imshennik VK, Novichihin SV, Matveev VV, Lyubutin IS (2012) Magnetic properties of monodisperse nanomagnetite. Russ J Phys Chem B 6:163–168. https://doi.org/10.1134/S1990793112010228

Swamy V, Dubrovinsky LS, Tutti F (1997) High-temperature raman spectra and thermal expansion of wollastonite. J Am Ceram Soc 80:2237–2247. https://doi.org/10.1111/j.1151-2916.1997.tb03113.x

Taleb K, Markovski J, Milosavljević M, Marinović-Cincović M, Rusmirović J, Ristić M, Marinković A (2015) Efficient arsenic removal by cross-linked macroporous polymer impregnated with hydrous iron oxide: material performance. Chem Eng J 279:279–278. https://doi.org/10.1016/j.cej.2015.04.147

Taleb K, Markovski J, Veličković Z, Rusmirović J, Rančić M, Pavlović V, Marinković A (2016a) Arsenic removal by magnetite-loaded amino modified nano/microcellulose adsorbents: effect of functionalization and media size. Arab J Chem. https://doi.org/10.1016/j.arabjc.2016.08.006

Taleb KA, Rusmirović JD, Rančić MP et al (2016b) Efficient pollutants removal by amino-modified nanocellulose impregnated with iron oxide. J Serbian Chem Soc 81:81–1213. https://doi.org/10.2298/JSC160529063T

Tejedor-Tejedor MI, Anderson MA (1990) The protonation of phosphate on the surface of goethite as studied by CIR-FTIR and

electrophoretic mobility. Langmuir 6:602–611. https://doi.org/10.1021/la00093a015

Veličković Z, Vuković GD, Marinković AD, Moldovan MS, Perić-Grujić AA, Uskoković PS, Ristić MĐ (2012) Adsorption of arsenate on iron(III) oxide coated ethylenediamine functionalized multiwall carbon nanotubes. Chem Eng J 181–182:174–181. https://doi.org/10.1016/j.cej.2011.11.052

Vuković GD, Marinković AD, Čolić M, Ristić MĐ, Aleksić R, Perić-Grujić AA, Uskoković PS (2010) Removal of cadmium from aqueous solutions by oxidized and ethylenediamine-functionalized multi-walled carbon nanotubes. Chem Eng J 157:238–248. https://doi.org/10.1016/j.cej.2009.11.026

Vuković GD, Marinković AD, Škapin SD, Ristić MĐ, Aleksić R, Perić-Grujić AA, Uskoković PS (2011) Removal of lead from water by amino modified multi-walled carbon nanotubes. Chem Eng J 173:855–865. https://doi.org/10.1016/j.cej.2011.08.036

Wang X, Mao H, Huang W, Guan W, Zou X, Pan J, Yan Y (2011) Preparation of magnetic imprinted polymer particles via microwave heating initiated polymerization for selective enrichment of 2-amino-4-nitrophenol from aqueous solution. Chem Eng J 178:85–92. https://doi.org/10.1016/j.cej.2011.10.015

Wang Y, Li B, Zhou Y, Jia D (2009) In situ mineralization of magnetite nanoparticles in chitosan hydrogel. Nanoscale Res Lett 4:1041–1046. https://doi.org/10.1007/s11671-009-9355-1

White SN (2009) Laser Raman spectroscopy as a technique for identification of seafloor hydrothermal and cold seep minerals. Chem Geol 259:240–252. https://doi.org/10.1016/j.chemgeo.2008.11.008

Zach-Maor A, Semiat R, Shemer H (2011) Adsorption–desorption mechanism of phosphate by immobilized nano-sized magnetite layer: interface and bulk interactions. J Colloid Interface Sci 363:608–614. https://doi.org/10.1016/j.jcis.2011.07.062

Zeng B, Yang L, Zheng W, et al (2017) Analysis of the formation process and performance of magnetic Fe_3O_4@poly(4-vinylpyridine) absorbent prepared by in-situ synthesis. J Mater Sci Technol In press,: doi: https://doi.org/10.1016/j.jmst.2017.07.007

Zeng L, Chen Y, Zhang Q, Guo X, Peng Y, Xiao H, Chen X, Luo J (2015) Adsorption of Cd(II), Cu(II) and Ni(II) ions by cross-linking chitosan/rectorite nano-hybrid composite microspheres. Carbohydr Polym 130:333–343. https://doi.org/10.1016/j.carbpol.2015.05.015

Zhao J, Zhu YJ, Wu J, Zheng JQ, Zhao XY, Lu BQ, Chen F (2014) Chitosan-coated mesoporous microspheres of calcium silicate hydrate: environmentally friendly synthesis and application as a highly efficient adsorbent for heavy metal ions. J Colloid Interface Sci 418:208–215. https://doi.org/10.1016/j.jcis.2013.12.016